

AD-A185 712

POST STALL BEHAVIOR IN AXIAL-FLOW COMPRESSORS(U)
VIRGINIA POLYTECHNIC INST AND STATE UNIV BLACKSBURG
CENTER FO W F O'BRIEN 20 AUG 87 WFOB/87-0801

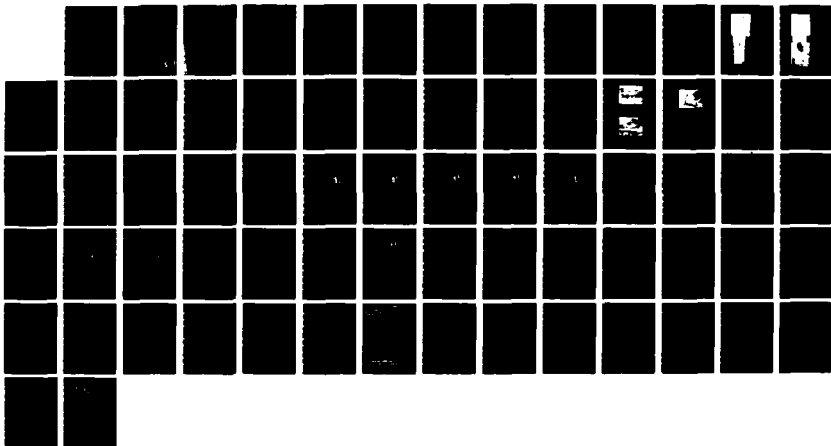
1/1

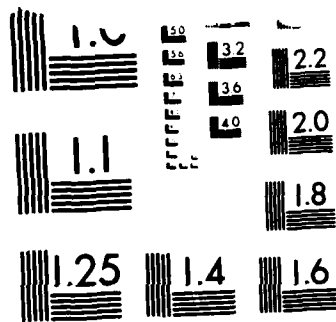
UNCLASSIFIED

AFOSR-TR-87-1195 F49620-83-K-0024

F/G 20/4

NL





MICROCOPY RESOLUTION TEST CHART
NATIONAL BUREAU OF STANDARDS-1963-A

AD-A185 712

REPORT DOCUMENTATION PAGE

UNCLASSIFIED		1b. RESTRICTIVE MARKINGS	
2a. SECURITY CLASSIFICATION AUTHORITY		3. DISTRIBUTION/AVAILABILITY OF REPORT	
2b. DECLASSIFICATION/DOWNGRADING SCHEDULE		Unlimited	
4. PERFORMING ORGANIZATION REPORT NUMBER(S) WFOB/87-0801		5. MONITORING ORGANIZATION REPORT NUMBER(S) AFOSR-TR- 87-1195	
6a. NAME OF PERFORMING ORGANIZATION Virginia Polytechnic Institute and State University		7a. NAME OF MONITORING ORGANIZATION Air Force Office of Scientific Research	
6b. OFFICE SYMBOL (If applicable)		7b. ADDRESS (City, State and ZIP Code) Bolling Air Force Base, DC-20332	
6c. ADDRESS (City, State and ZIP Code) Blacksburg, VA 24060		7c. ADDRESS (City, State and ZIP Code) Bolling Air Force Base, DC-20332	
8a. NAME OF FUNDING/SPONSORING ORGANIZATION NA Bolling AFB, DC 20332		9. PROCUREMENT INSTRUMENT IDENTIFICATION NUMBER F49620-83-K-0024	
8b. OFFICE SYMBOL (If applicable) NA		10. SOURCE OF FUNDING NOS.	
8c. ADDRESS (City, State and ZIP Code) Bolling AFB, DC 20332		PROGRAM ELEMENT NO.	TASK NO.
		PROJECT NO.	WORK UNIT NO.
11. TITLE (Include Security Classification) Post Stall Behavior in Axial Flow Compressors (unclassified)		61102F	2307 A1
12. PERSONAL AUTHOR(S) O'Brien, Walter F.			
13a. TYPE OF REPORT Final	13b. TIME COVERED FROM 83/03 TO 87/01	14. DATE OF REPORT (Yr., Mo., Day) 87/08/20	15. PAGE COUNT 69
16. SUPPLEMENTARY NOTATION			
17. COSATI CODES		18. SUBJECT TERMS (Continue on reverse if necessary and identify by block number)	
FIELD	GROUP	Compressors, Cascades, Flow Measurements, Stalling Behavior, Propagating Stall	
	SUB. GR.		
19. ABSTRACT (Continue on reverse if necessary and identify by block number)			
<p>A multi-element research program was conducted to improve understanding of the role of cascade losses in compressor post-stall behavior. Experiments in a special wind tunnel designed for high-angle-of-attack investigations included surface and smoke flow visualizations and hot film anemometer velocity measurements. Results showed the details of the stall development in a cascade, and the effect of stagger on measured flow losses. Predictions of a Navier-Stokes model for separated cascade flows were compared with experimental results. An improved compressor stage model predicts post-stall characteristics, and illustrates the application of the results to compression system analysis.</p>			
20. DISTRIBUTION/AVAILABILITY OF ABSTRACT UNCLASSIFIED/UNLIMITED <input checked="" type="checkbox"/> SAME AS RPT. <input type="checkbox"/> DTIC USERS <input type="checkbox"/>		21. ABSTRACT SECURITY CLASSIFICATION Unclassified	
22a. NAME OF RESPONSIBLE INDIVIDUAL Dr. James Wilson		22b. TELEPHONE NUMBER (Include Area Code) 202/767-4935	22c. OFFICE SYMBOL AFOSR/NA

DTIC
ELECTE
OCT 07 1987
S
R
E

FINAL REPORT

POST STALL BEHAVIOR IN AXIAL-FLOW COMPRESSORS
AFOSR Contract F49620-83-K-0024

Center for Turbomachinery and Propulsion Research
Virginia Polytechnic Institute and State University
Blacksburg, Virginia 24061

Professor Walter F. O'Brien
Principal Investigator

for

Air Force Office of Scientific Research
Bolling Air Force Base, DC

Dr. James Wilson
Technical Monitor



Accession For	
NTIS GRA&I	<input checked="" type="checkbox"/>
DTIC TAB	<input type="checkbox"/>
Unannounced	<input type="checkbox"/>
Justification	
By _____	
Distribution/	
Availability Codes	
Dist	Avail and/or Special
A-1	

August 1987

CONTENTS

1.0	BACKGROUND	4
2.0	THE RESEARCH PROGRAM	6
3.0	SUMMARIZED RESULTS	9
3.1	Cascade Tests	9
3.1.1	Surface Flow Visualization	10
3.1.2	Reynolds Number Effects	17
3.1.3	Tip Clearance Effects	18
3.1.4	Conclusions, Surface Flow Visualization	20
3.1.5	Smoke Flow Visualization Results	21
3.1.6	Test Section Inlet Mean Velocity Measurements	28
3.1.7	Turbulence Intensity Measurements	29
3.1.8	Velocity Measurements and Numerical Predictions	30
3.1.9	Cascade Pressure Measurements	45
3.1.10	Cascade Performance	46
3.1.11	Conclusions, Cascade Measurements	51
3.2	Prediction of Separated Flow in Cascades	55
3.3	Improvements in Post-Stall Compressor Stage Model	55
4.0	PUBLICATIONS	55
5.0	GRADUATE STUDENTS PARTICIPATING IN THE PROGRAM	59
6.0	INTERACTIONS AS A PART OF THE PROGRAM	59
7.0	REFERENCES	59
8.0	APPENDIX	61

FINAL REPORT

RESEARCH PROJECT
"POST STALL BEHAVIOR IN AXIAL-FLOW COMPRESSORS"
AFOSR CONTRACT NO. F49620-83-K-0024
Dr. James Wilson, Technical Monitor
Prof. W. F. O'Brien, Principal Investigator

August, 1987

1.0 BACKGROUND

This program was conceived and has been carried out to provide fundamental insight into the cascade stalling process and related post-stall behavior in the axial-flow compressors of aircraft gas turbine engines.

The multi-stage axial-flow compressor has undergone continuous and successful development by the aircraft engine community over the past 40 years. High pressure ratios with high efficiency have been obtained, and means to produce adequate stability margin have been developed and employed. Dual-spool designs, variable stagger stators, compressor bleed ports, and rotor casing tip treatment have been employed separately or in combinations to increase compressor stability margin over the engine speed range. While the compressor stability margin, shown graphically in Fig. 1, has been the object of much interest and research, less is known about the post-stall operating line.

If the compressor stability margin is exceeded as a result of unsteady or off-design engine operation, a surge or a rotating stall is the result, depending on the presently well-known system and compressor operating parameters. The compressor can operate continuously on the post-stall operating line if rotating stall is the result of exceeding the stability margin.

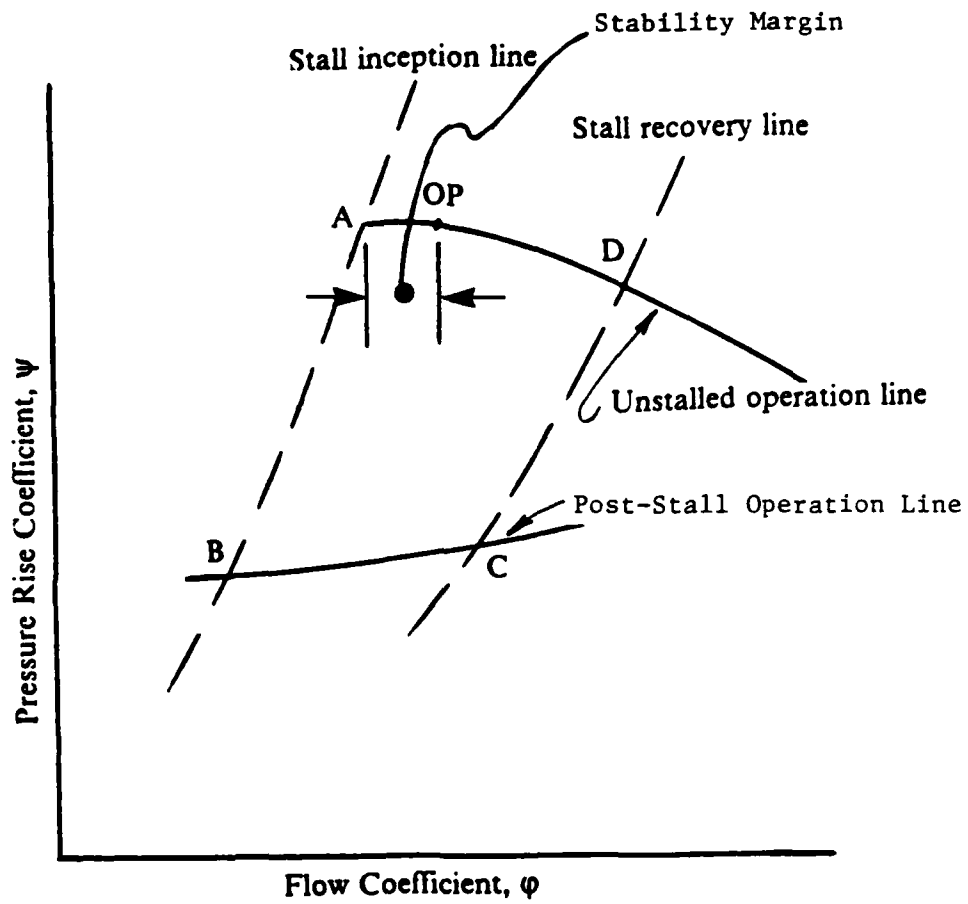


Fig. 1 Compressor Operating Characteristic

The rotating stall phenomenon has been extensively investigated both analytically and experimentally. The fluid mechanics involved are very complex, and it has never been possible to accurately predict the exact inception point, the number and speed of the cells, or the post-stall operating and recovery line. Improved understanding of rotating stall and compressor post-stall behavior through fundamental experimental investigation was the goal of the present research.

2.0 THE RESEARCH PROGRAM

Prior to the present research program, the Principal Investigator had carried out research on rotating stall and recovery characteristics employing a mathematical model¹. The model gave indications that the fluid dynamic losses of the compressor blade row were of principal importance in determining the post-stall and recovery characteristic. Extensive searches of the literature showed that there was almost no data on the development of losses in compressor cascades operated at the high angles of attack associated with rotating stall. Virtually all data sets ended at an angle of attack which produced twice the minimum losses, far less than was necessary to investigate the role of cascade losses in compressor post-stall behavior. It was desirable to conduct additional research to obtain the loss data necessary to evaluate the predictions of the model, and to understand the developing and limiting stalling process in the compressor cascade.

The program objectives included the further development of the compressor post-stall mathematical model as a tool to understand the role of cascade losses in post-stall behavior, the modification of a cascade wind tunnel for experimental research, and the

measurement of cascade losses over a wide range of angle of attack for three stagger angles typical of modern compressor design. With the data and the improved model, it was anticipated that some understanding of the underlying fluid mechanics of post-stall behavior could be deduced, and that the hypothesis of the principal role of cascade losses in determining that behavior could be checked.

To pursue program objectives, planned activities were organized under three tasks, as follows:

Task 1, Cascade Tests - The VPI high-angle-of-attack cascade test facility shown in Fig. 2 was to be employed for experimental investigations. Initial tests verified that accurate cascade loss and turning angle data could be obtained for flow angles well in to the stalling regime². Employing the circular arc airfoils installed in the facility, loss and turning angle data were to be obtained for three stagger angle settings, 25, 36.5 and 45 degrees. The 36.5 degree setting corresponded to the stagger angle of the VPI high speed compressor rig, for which stalling data was available. In addition to the basic data, blade pressure profiles and the general nature of the observed flow separation were to be recorded.

Task 2, Prediction of Separated Flow in Cascades - While the cascade experiments were expected to produce valuable results, it was ultimately desired to develop prediction techniques for unsteady, stalling flows in cascades. Starting from the referenced analysis by H. Moses², it was planned to develop a cascade flow analysis which accurately predicted post-stall flow behavior.

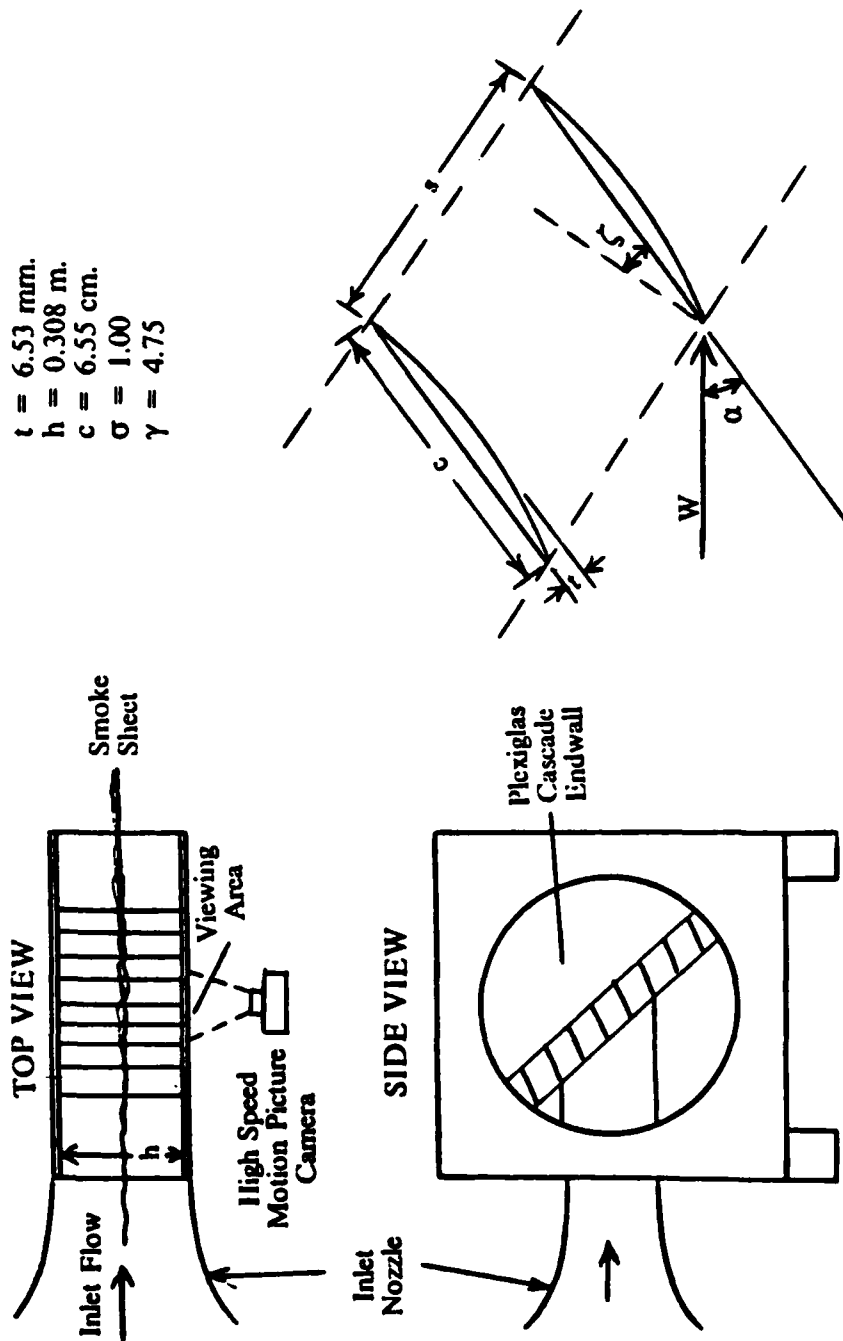


Fig. 2 Cascade Geometry

Task 3, Improvements in the Model for Post-Stall Response in Compressors - The compressor model was needed to evaluate the information gained from the cascade flow analysis and experiments for relevance to compressor stage performance. Certain improvements to the present model were desirable. These included improvements in the method for applying the dynamic response function to cascade data, incorporation of a means for calculating circumferential static pressure variation, and the addition of a global calculation for prediction of compressor flow and pressure rise.

3.0 SUMMARIZED RESULTS

Results obtained in the program are organized according to the Tasks listed above.

3.1 Cascade Tests

The high-angle-of-attack cascade tunnel was suitably configured, and fundamental experiments to determine the nature of the stalling process and loss development were conducted. It was planned to measure the fluid losses with pneumatic probes, following the determination of local flow directions with hot film probes. An extensive program of flow visualization was undertaken, so that the point measurements of the probes could be properly interpreted. The flow visualization work provided some of the most important results of the investigation.

3.1.1 Surface Flow Visualization

Oil-film surface flow visualization was used to study the blade surface flow features with high-angle-of-attack flows. In the full report of this work³, approximately 50 sketches and photographs describe the results. Tests were conducted at stagger angles of 25, 36.5, and 45 degrees. A summary of the results are provided here.

Figures 3 and 4 show photographs of typical surface flow patterns produced by the cascade flows. From the patterns, observations concerning the boundary layer development and the nature of stalling in the cascade were deduced. A map summarizing the boundary layer development at the mid-span section of the cascade, for all stagger angles tested, is presented in Fig. 5. This figure was constructed from detachment and reattachment points measured directly from the blade surfaces. A general curve was fitted through these points to divide the different boundary layer regions.

At negative incidences, the blade row stagger appears to have little effect. Laminar flow exists on the suction surface for the first 60 percent chord, whereupon the boundary layer detaches completely. Separation occurs earlier as the angle of attack is increased. On the pressure surface, aside from the laminar separation bubble at the leading edge, the boundary layer is turbulent. The bubble region decreases with increasing angle of attack, and disappears as the incidence becomes positive, at which the flow is fully attached. The nature of the boundary layer could not be deduced from the visualizations, but the literature suggests it is mostly laminar.

For small positive incidences, a laminar separation bubble forms at

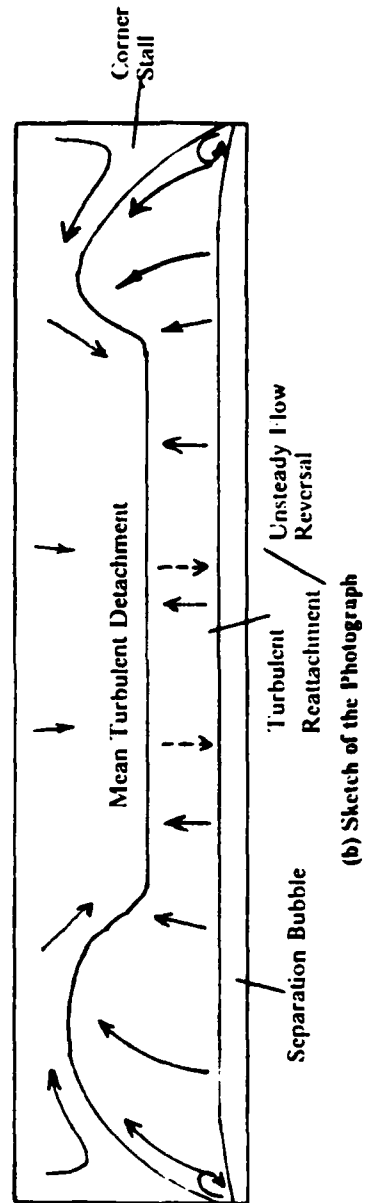
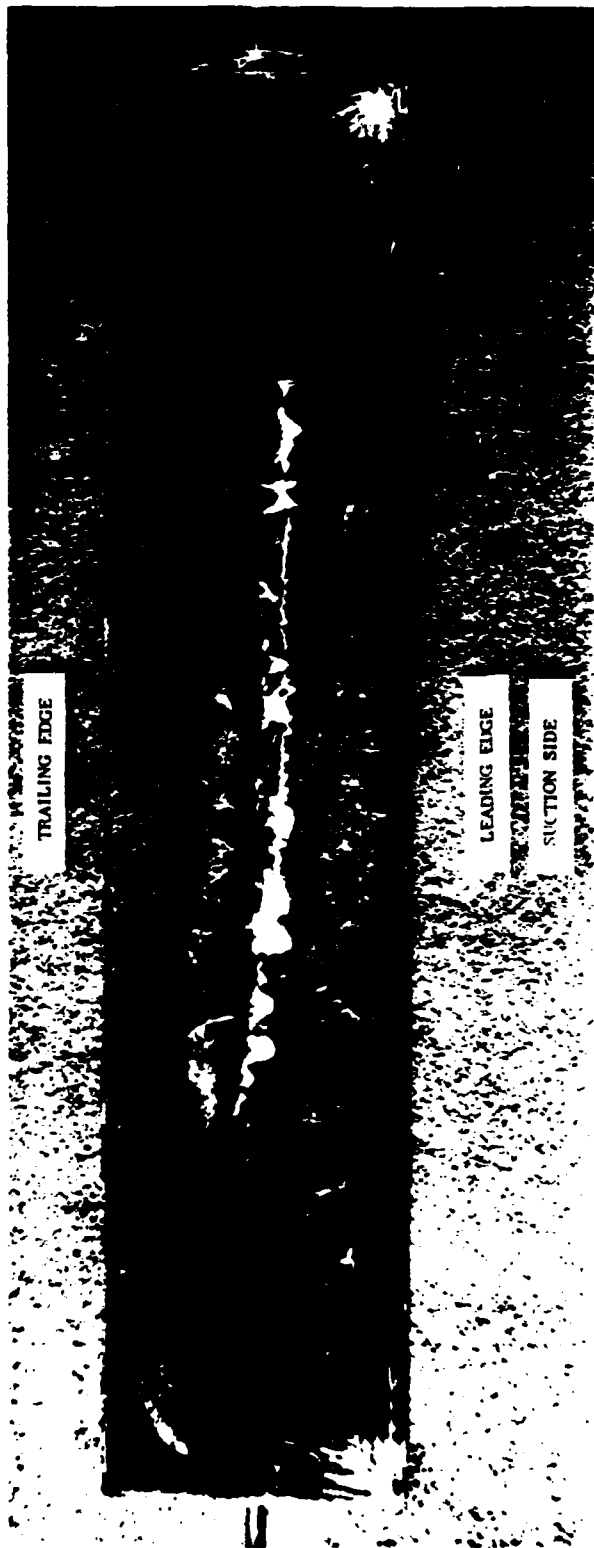
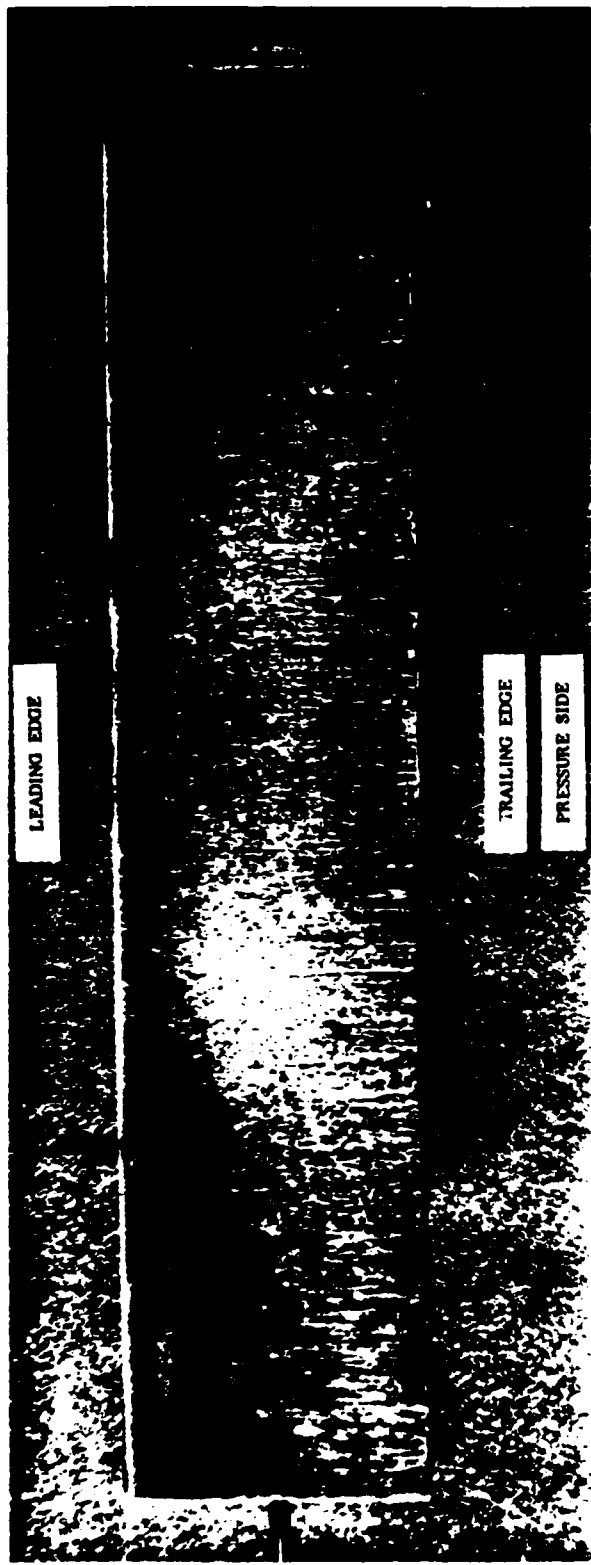
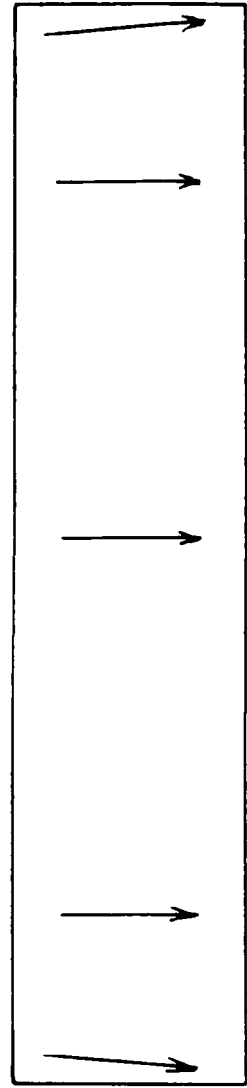


Figure 3. Surface Flow Pattern for $\xi = 36.5^\circ$ and $\alpha^* = 20^\circ$ (Suction Side)



(a) Photograph



(b) Sketch of the Photograph

Figure 4. Surface Flow Pattern for $\xi = 36.5^\circ$ and $\alpha^* = 20^\circ$ (Pressure Side)

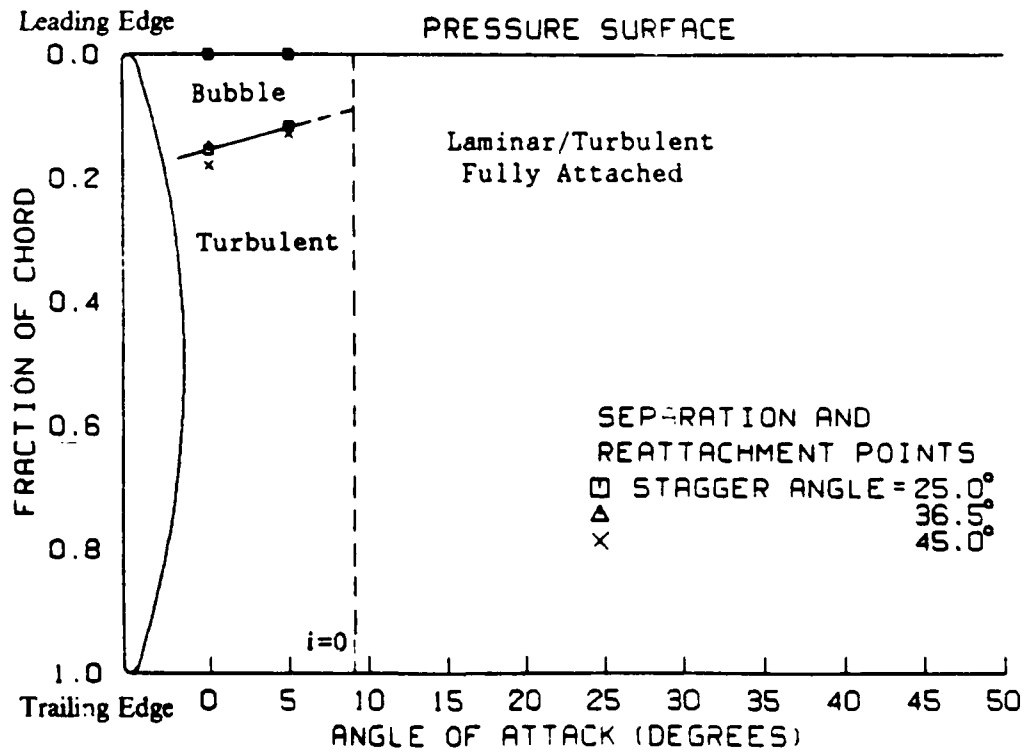
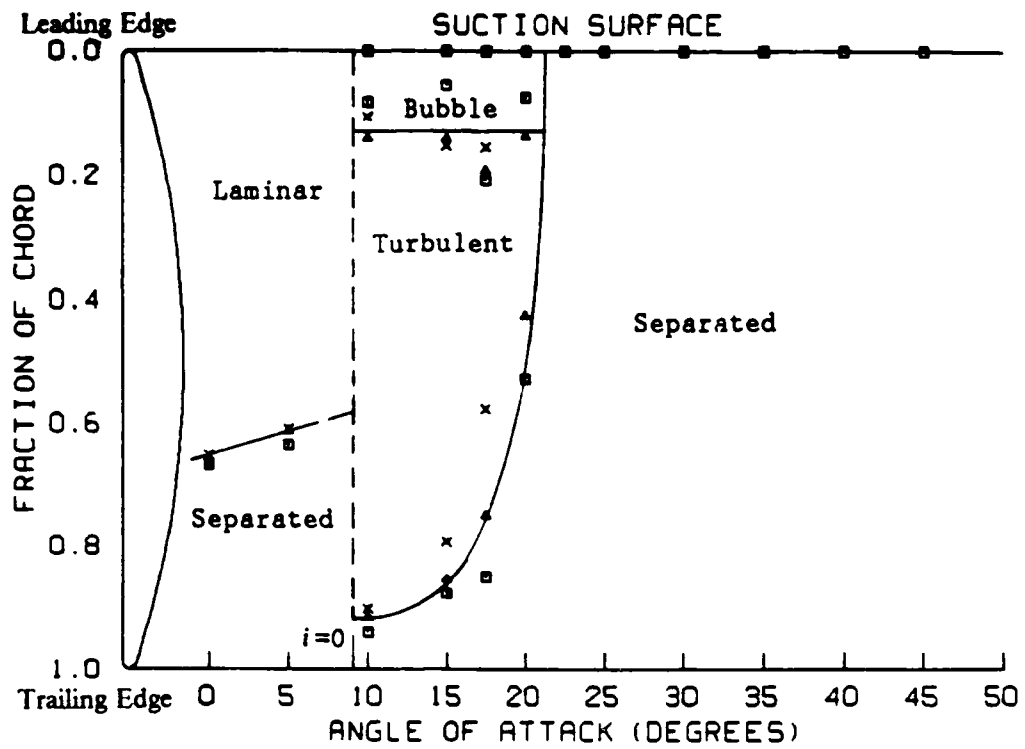


Figure 5. Summary of the Midspan Boundary Layer Development for $Re_c = 2.0 \times 10^5$ and $Tu = 1.1$ percent

the leading edge of the suction surface and remains present until stall is complete. The reattachment data show much scatter. It is felt that the bubble length did not actually change much with respect to angle of attack or stagger angle, and that the scatter is due to an error in measurement. The reattachment line in most cases was difficult to distinguish. Moreover, it is believed that the appearance of the leading edge separation bubble on the pressure surface at negative incidences and on the suction surface at positive incidences is due to the relative sharpness of the blade nose, and that its effect on the overall features of stall is insignificant.

The change in the blade surface flow characteristics as the angle of attack is varied from negative to positive incidence is believed to occur suddenly. No physical evidence was obtained in this work to fix the incidence of transition. However, as shown in the figure, it is reasonable to assume that transition occurs at zero incidence.

The predominant characteristic of the suction surface stall at positive incidence is the rapid progress of the turbulent separation zone toward the leading edge of the airfoil. The effect of the stagger angle is manifested in the severity of stall at equal angles of attack. The higher stagger cascade has a narrower operating range. At midspan, full stall occurred at an angle of attack near 20 degrees for the 45 degree stagger setting, and near 22.5 degrees for the two other staggers.

The general nature of the observed three-dimensional stalling process and surface flow under fully stalled conditions is summarized in schematic form in Fig. 6. Preceding and following the inception of

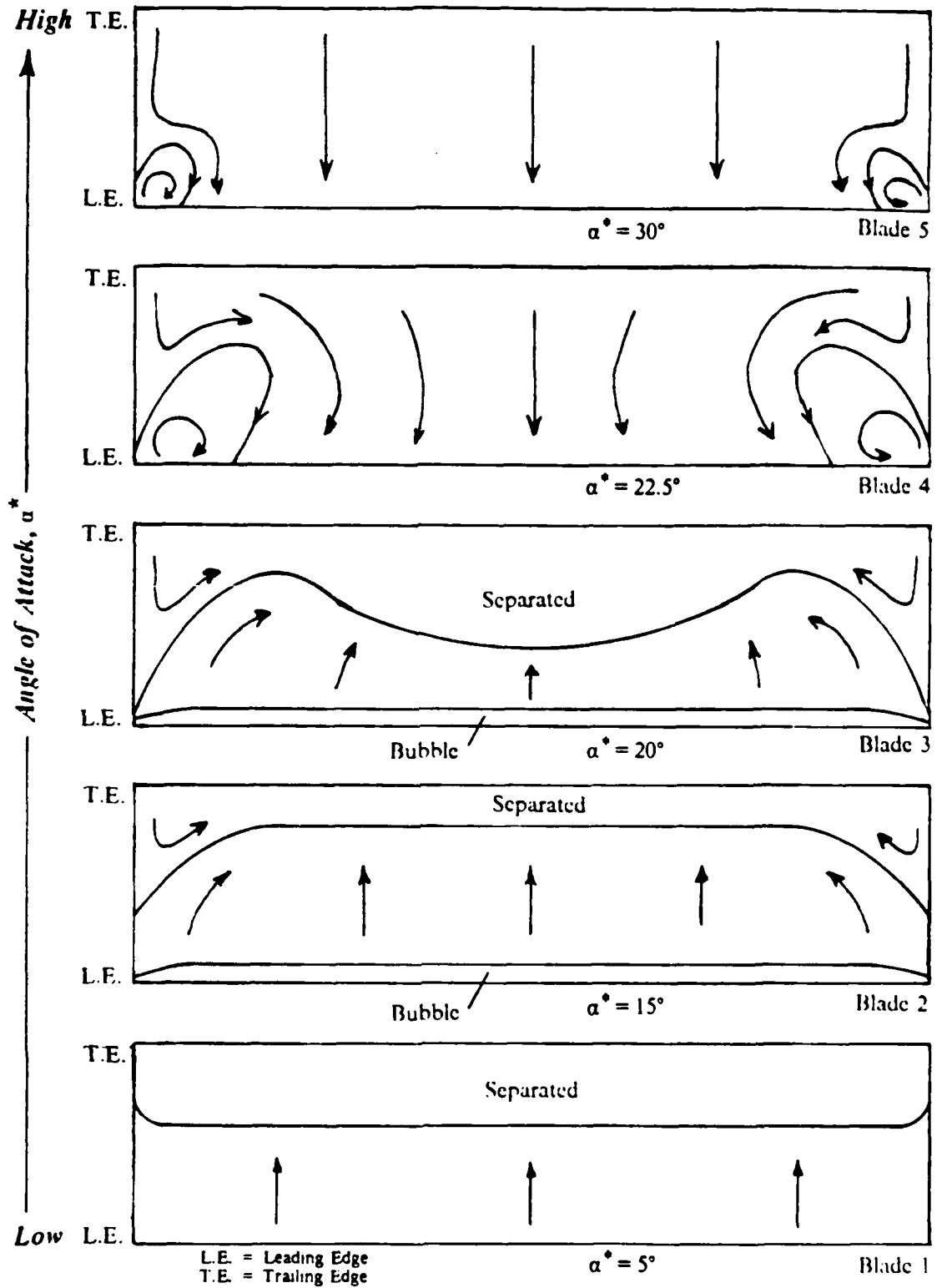


Figure 6. Summary of the Three-Dimensional Flow on the Blade Suction Surface

complete separation at the leading edge, the flow at the blade suction surface is essentially two-dimensional. Corner stall is the predominant mechanism for three-dimensionality preceding full stall. Corner stall appears at small positive incidence and becomes physically more severe with increases in the angle of attack. At operation near full stall, the turbulent separation was delayed by the corner stall, but because of the high aspect ratio blades used, this effect was concentrated in regions away from midspan. It is easy to imagine from these results how the turbulent separation in the midspan region would have been altered and delayed if a lower aspect ratio cascade had been employed in this investigation.

The observed boundary layer behavior was related to axial velocity ratio (AVR) measurements. It was found that an increase in the angle of attack resulted in a rise in the AVR. The rate of increase slowed in the fully stalled flow regime. The AVR data showed a maximum value of about 1.15. The rise in the AVR above unity paralleled the growth seen in the corner stall region. In the fully stalled flow regime, the diffusion by the cascade levels, as does the pressure rise, thereby limiting any further increase in the corner stall region and the AVR. Here, the surface streamlines were found to be straight for a large percentage of the blade height, but the AVR did not return to unity. This illustrates the possible error in describing tests as being truly two-dimensional based solely on surface flow visualization results.

3.1.2 Reynolds Number Effects

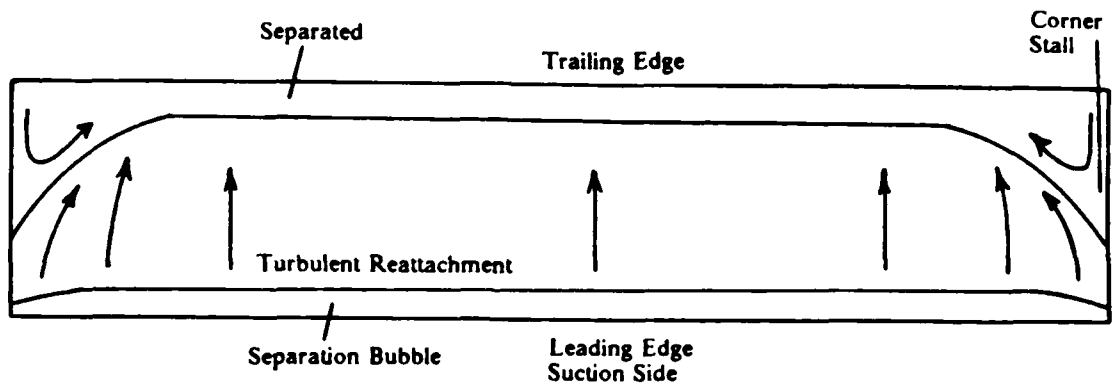
Additional blade surface flow visualization tests were conducted to provide physical evidence as to whether the test Reynolds number of 2.0×10^5 was above the critical Reynolds number range. This series of experiments was carried out with the blade cascade set at a stagger of 36.5 degrees. Visualizations were obtained for Reynolds number of 2.0×10^5 , 1.5×10^5 , and 1.0×10^5 at angles of attack of 5, 15, 20, 25, and 35 degrees. The Reynolds number was varied by adjusting the inlet velocity.

In summary, the rapid deterioration in the performance of a compressor cascade with decreasing Reynolds number is generally thought to result from the appearance and growth of laminar separation bubbles on the suction surface of the blades. The Reynolds number test results showed relatively small changes in boundary layer development with decreasing Reynolds number, and any increase in losses is believed to be minimal. The pressure surface flow showed no variation with Reynolds number. On the suction surface, some small increases occurred in the size of the laminar and turbulent separation zones. The leading edge separation bubble observed on the pressure surface at negative incidences, and on the suction surface at positive incidences, is believed to be due to the relative sharpness of the blade nose and is not a Reynolds number effect. The only real doubt as to whether the Reynolds number of 2.0×10^5 is above the critical range involves laminar separation observed on the suction surface at negative incidences. It is possible that at a higher Reynolds number, only a partial separation would be obtained with turbulent reattachment.

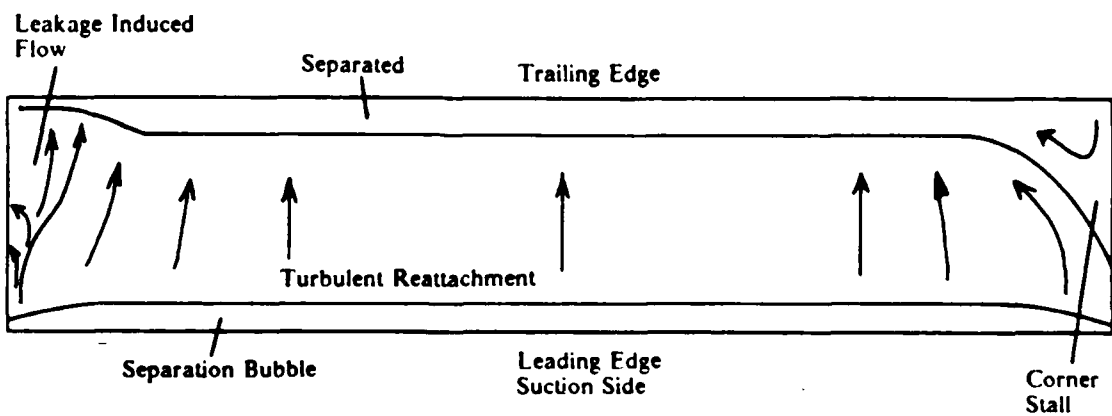
3.1.3 Tip Clearance Effects

Surface flow visualization was used to investigate the effects of tip clearance on boundary layer development across the blade span. For this investigation, bridge pieces were removed from the test section leaving a clearance of gap/chord ratio equal to 4.8 percent between the left sidewall and blade tips. With the blade cascade set at a stagger angle of 36.5 degrees, tests were performed at angles of attack of 15, 20, 25, and 30 degrees. Sample sketches of the blade surface flow patterns obtained with and without tip clearance are shown in Fig. 7. In the figure, the gap end is to the left. Additional photos and sketches are shown in Ref. 3.

In summary, at positive incidences prior to full stall, tip leakage was very effective in preventing the premature separation on the blade surface associated with corner stall. Separation was actually delayed for a short distance from the gap. This distance increased somewhat with increasing angle of attack. Inward of the region under the direct influence of the leakage flow, the limiting streamlines converged towards midspan, but at an angle somewhat less than that caused by corner stall with zero clearance. For operation in the fully-stalled region, the gap produced some unstalled flow near the gap, but for all practical purposes the effect was considered small. Further, a three-dimensional flow resulted at the gap end which was equal in extent to that found at the zero clearance end.



(a) Zero Clearance



(b) Clearance/Chord = 4.8 percent

Figure 7. Sketches of the Surface Flow Patterns Showing Tip Clearance Effects for $\xi = 36.5^\circ$ and $\alpha^* = 15^\circ$

3.1.4 Conclusions, Surface Flow Visualization

Oil-flow visualizations were conducted in a solid wall, high aspect ratio, compressor cascade for the purpose of describing the transition from corner stall to full blade stall, and the blade surface flow under fully stalled conditions. Results were obtained for stagger angles of 25, 36.5, and 45 degrees.

Similar trends in boundary layer development were exhibited for the three stagger angles. At negative incidences, the suction surface showed substantial areas of laminar flow. The laminar boundary layer terminated in a complete separation of flow from the blade surface. On the pressure surface a laminar separation bubble existed at the leading edge with the remaining boundary layer turbulent.

At small positive incidences a laminar separation bubble developed at the leading edge of the suction surface, followed by turbulent reattachment a short distance downstream. The turbulent boundary layer separated near the trailing edge. As the angle of attack was increased to the point of a complete leading edge separation, the turbulent separation progressed upstream, with no large changes in the laminar bubble. The boundary layer on the pressure surface was fully attached for the range of positive incidences tested; the boundary layer structure could not be determined from the experiments.

The effects of stagger were revealed in the severity of the stall at positive incidences. Transition to complete separation at the leading edge occurred at lower angles of attack for the higher stagger angles.

The most interesting discoveries from the work deal with the

profile boundary layer three-dimensionality. Geometrically speaking, the flow on the pressure surface was found to be virtually two-dimensional for all tested angles of attack. The suction surface flow was shown to be essentially two-dimensional preceding and following the transition to a fully separated flow at the leading edge. Corner stall was observed at small positive incidence and grew in severity with increasing angles of attack. Near full stall at midspan, turbulent separation was delayed in regions adjacent to the corner stall zones. For fully-stalled conditions, the three-dimensional mechanism took the form of recirculating flow regions at the ends of the blades.

Special oil-flow tests were conducted to study Reynolds number and tip clearance effects on the blade boundary layer development under normal and fully-stalled conditions. No pronounced changes in boundary layer development were observed in the Reynolds number range from 1.0×10^5 to 2.0×10^5 . The tip clearance tests showed for this cascade that the gap/chord ratio of 4.8 prevented corner stall and actually delayed turbulent separation for some distance from the gap. After the flow was fully separated, the gap had only small effects concentrated near the end of the blade.

3.1.5 Smoke Flow Visualization Results

Smoke flow visualization tests were conducted to qualitatively examine the nature of the stalled flow and to determine the existence and type of unsteadiness. Separated flows are usually unsteady. However, an ordered unsteadiness in the form of a propagating stall could also exist when testing cascades of airfoils. The existence and

type of unsteadiness is important in itself, particularly if design variables affect the occurrence of propagating stall and the propagating speed. It was also important to know if the flow was unsteady when evaluating the data from the pressure and velocity measurements.

Still shot photographs were initially taken over a range of angle of attack for the cascade with a 36.5 degree stagger. These photographs were taken to determine if high speed photography would reveal the flow structures of interest. With the high velocity of the flow, the unaided eye could not, at the very least, resolve the separated regions and obviously could not identify the unsteadiness. The separated flow regions were visible when strobe lights were used to illuminate and slow the flow. However, the unsteadiness still could not be observed. Figures 8, 9, and 10 are photographs of the flow at 15, 25, and 35 degrees angles of attack. The flow in the photographs was frozen by using seven Strobotacs to provide the flash. These strobes lights were connected in parallel and triggered by the camera.

In Fig. 8 the smoke reveals the free stream turbulence and a possible small separated region near the trailing edge of the airfoil. For this angle of attack the boundary layers appear to be attached over most of the blade. Mixing in the wake of the airfoils is evident from the more diffuse smoke in this region.

Figures 9 and 10 show the flow for angles of attack of 25 and 35 degrees, respectively. For both of these photographs, large separated regions are evident. It appears that the flow separates from the leading edge of the blades and that the size of the separated region increases (as expected) with an increase in angle of attack. It is also



Figure 8. Photograph of the smoke flow visualization for $\xi = 36.5^\circ$ and $\alpha = 15^\circ$

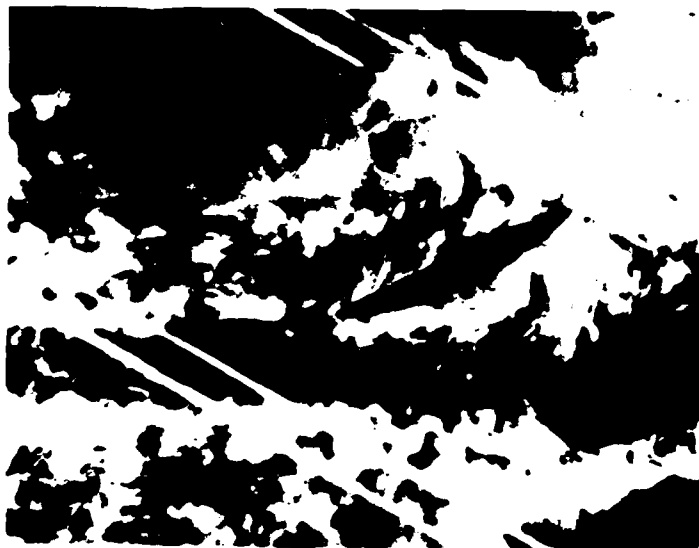


Figure 9. Photograph of the smoke flow visualization for $\xi = 36.5^\circ$ and $\alpha = 25^\circ$

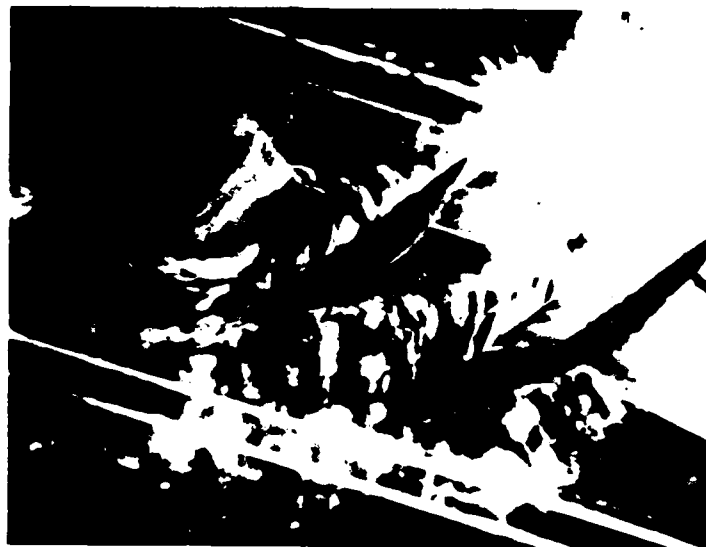


Figure 10. Photograph of the smoke flow visualization for $\xi = 36.5^\circ$ and $\alpha = 35^\circ$

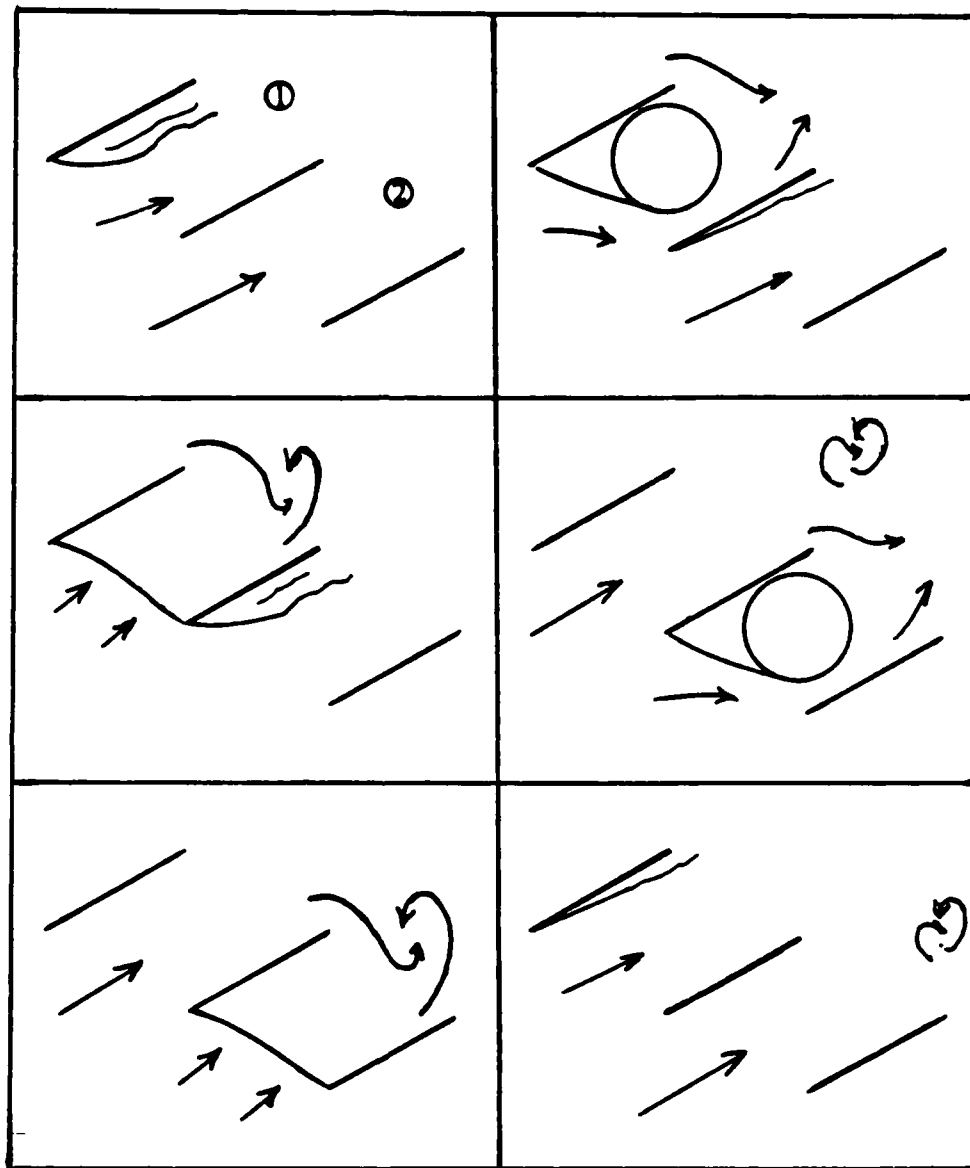
evident in both Figs. 9 and 10 that the separated regions at this instant in time are not identical in the two neighboring passages. In Fig. 9 the separated region in the middle passage is larger than the separated region in the passage below, and has diffuse smoke in the entire region. In the passage below the middle passage, the separated region is smaller. The differences observed in the two passages of Fig. 9 are similar to what would be expected if propagating stall was present. However, conclusive evidence with regard to the existence of propagating stall would require sequential photographs taken at very short intervals (or high speed motion pictures).

The still shot photographs verified that the structure of the flow could be observed with the present smoke visualization system. However, it also became apparent that high speed movies would be necessary to determine if propagating stall occurs. A Hycam II high speed rotating prism camera was used to photograph the flow at 4000 frames per second. Motion pictures of the flow were created for test cases covering a full range of angle of attack and for staggers of 25, 36.5, and 45 degrees. For selected cases, film was taken for high and low inlet velocities corresponding to Reynolds numbers of approximately 200,000 and 70,000.

Viewing the films at a normal projection speed of 16 frames/second slowed the flow by a factor of 250 to 1. For the 25 degree stagger cascade, propagating stall was not observed even at angles of attack as large as 45 degrees. For the cascades with staggers of 36.5 and 45 degrees, propagating stall was observed at all angles of attack of 20 degrees and greater. Contrary to what may have been expected, the flow did not restabilize at high angles of attack, but continued to reveal

propagating stall superimposed on a mean full stall from the leading edge. The propagating stall evident in the films showed the classical blockage of a passage, the flow diversion upstream of the cascade around the blockage, and the subsequent recovery (or complete flushing out) in the passage behind the propagating cell. Ahead of the stall cell, the increase in angle of attack caused by the flow diverting around the blockage resulted in the next blade stalling. It was also observed that stall propagation was associated with almost complete blockage of a passage and not just an increase in blockage from the mean. In the 25 degree stagger cascade, the stall did not propagate, and in this case the passage was observed to never be completely blocked.

Piatt⁴ examined the films which were created in this study in detail. He determined the number of occurrences of stall propagation and the propagation speeds for each test case with the 36.5 and 45 degree stagger cascade. The complete results of his study are presented in Ref. 4, along with groups of sequential frames from the films to provide supporting evidence. Figure 11 is a summary of Piatt's observations of the history of a typical propagating stall event. He concluded that the propagation speed was nearly proportional to the inlet velocity. A small decrease in the propagation speed was observed at 20 degrees of angle of attack, which was associated with the occurrence of slightly less than complete blockage of the passage. Once an angle of attack was reached where the passage became fully blocked, no further changes in the propagation speed occurred.



Picture 1
Picture 3
Picture 5

Picture 2
Picture 4
Picture 6

Figure 11. Observed Sequence of Events in Propagating Stall

3.1.6 Test Section Inlet Mean Velocity Measurements

Russ [3] conducted surveys of the velocity field upstream of the cascade for the purpose of evaluating the uniformity of the flow. Surveys were made from side wall to side wall in the spanwise direction and over a distance of 4 blade spacings in the pitch direction. Russ' measurements showed that the flow in the spanwise direction is uniform within 1 m/s outside of the wall boundary layers. The boundary layers on the side walls vary in thickness from approximately 14 mm to 29 mm, depending on which wall is considered and the pitch location of the measurement. Even for the maximum measured boundary layer thickness of 29 mm, the blades, which have a span of 308.0 mm, are subjected to uniform flow over 81% of the span. Thus, highly uniform inlet flow in the span direction was present during the tests.

Russ conducted upstream pitchwise traverses at three span locations and three Reynolds numbers. All traverses exhibited an approximately sinusoidal variation in the velocity, with a wavelength equal to the blade spacing. Since the traverses were conducted at a 25 degree angle of attack, the upstream variation in velocity can be attributed to the divergence around the regions blocked by stalled flow. The peak amplitude of the velocity variation had its greatest value of approximately 3% of the mean velocity for the tests with the largest inlet velocity.

Another means of evaluating the periodicity of the flow is by measuring the pressure from the static wall taps located upstream of the cascade. These taps were spaced at intervals equal to one blade spacing, and thus periodic flow would be indicated by equal pressures.

Measurements of the pressures from these taps were made during the pressure measurement series of tests. A variation in static pressure from the top to the bottom does exist for every nonzero cascade inlet angle, α_1 . The variation is simply the result of the lower taps being at a greater distance downstream of the nozzle, where a larger pressure drop has occurred due to viscous friction in the boundary layers. Because of the source of the variation, it would be expected to have the greatest variation at the higher inlet angles. For the maximum inlet angle of $\alpha_1 = 75$ degrees, the difference in static pressure between the taps located five spacings apart is 11.2 mm H₂O. This corresponded to only 8.5% of the inlet dynamic head for this worst case. At the minimum inlet angle tested, $\alpha_1 = 25$ degrees, the difference in static pressure over three blade spacings was 3.49 mm H₂O, which was 3% of the inlet dynamic head. For the purpose of modeling two-dimensional cascade flow, the inlet velocity field was therefore shown to be uniform in the spanwise direction and essentially periodic in the pitchwise direction.

3.1.7 Turbulence Intensity Measurements

Free stream turbulence intensity levels are known to affect the boundary layer transition, the type and location of separation and, consequently, the performance of a compressor blade row. Although it is not necessary to minimize the freestream turbulence, it is important to measure the turbulence in order to completely characterize the inlet conditions. The turbulence intensity, $\frac{\sqrt{u'^2}}{\bar{u}}$, was measured at an array of points for four different inlet velocities corresponding to Reynolds number based on the blade chord of 200000, 150000, 100000, and 57000.

The array of measurement locations consisted of three span locations of $z = 79, 156, \text{ and } 232 \text{ mm}$. At each span position, measurements were made at 25.4 mm increments in the pitch direction. These data were obtained with a cascade stagger angle of 45 degrees and an angle of attack of 10 degrees . Preliminary tests at an angle of attack of 25 degrees exhibited severe unsteadiness, probably as a result of propagating stall.

The turbulence intensities ranged from $1.1 \text{ to } 1.3\%$ for all inlet velocities and measurement locations. The variation in the intensity was relatively small and was considered insignificant. The point to point variation in mean velocity was less than 1 m/s .

3.1.8 Velocity Measurements and Numerical Predictions

The magnitude and angles of the flow velocity in the cascade were obtained experimentally from measurements with the dual split film probe. The time mean flow angles downstream of the cascade were the main quantities of interest, being required to align the pneumatic probe with the flow in the subsequent experiments. For angles of attack of $15, 20, 25, \text{ and } 30 \text{ degrees}$, surveys across the passage at approximately 20% and 50% chord were also conducted to further define the extent of the separated region within the blade passage. The four signals from the hot film probe were processed to produce a velocity measurement, and twenty measurements were averaged at each point. Plots of the averaged velocity vectors provide a pictorial indication of what the flow is like through the cascade. Figures 12 through 23 show the measured velocity

vectors. All the data presented in these figures is for a nominal Reynolds number of 200000.

For a given stagger angle, the variation of the flow fields with angle of attack are consistent with the expected trends. At the lower angle of attack of 15 degrees, Figs. 12, 16, and 20 show no reverse flow indicated by the measured vectors, and the vectors increase in magnitude as the suction surface is approached. The acceleration of the flow near the suction surface is a potential flow effect which results in the creation of lift on the airfoil. As the angle of attack is increased to 20 degrees, Figs. 12, 17, and 21 show that viscous effects near the suction surface have increased, resulting in a much larger boundary layer on the blades and a larger wake downstream. At this angle of attack, no reverse flow is indicated by the measurements, although separated flow was indicated to some extent by the surface flow visualization. Therefore, it can be assumed that measurements at this angle of attack could not be made near enough to the surface to resolve the separated flow region.

The results for angles of attack of 25 and 30 degrees are given in Figs. 14 and 15, 18 and 19, and 22 and 23. At these angles of attack the measurements for all three stagger angles indicate reversed flow. The separated flow regions are seen to increase in size as the angle of attack is increased from 25 to 30 degrees.

The most significant observation to be made from Figs. 12 through 23 is the change in the nature of the flow associated with the changes in stagger angle. For the cascade with a stagger of 25 degrees, Figs. 14 and 15 show that two distinct regions exist within the blade

TEST NOS. CT31, BB04, BB05
STAGGER ANGLE: 25.0
ANGLE OF ATTACK: 15.0
INLET VELOCITY: 159.8 FT/SEC
REYNOLDS NUMBER: 199939

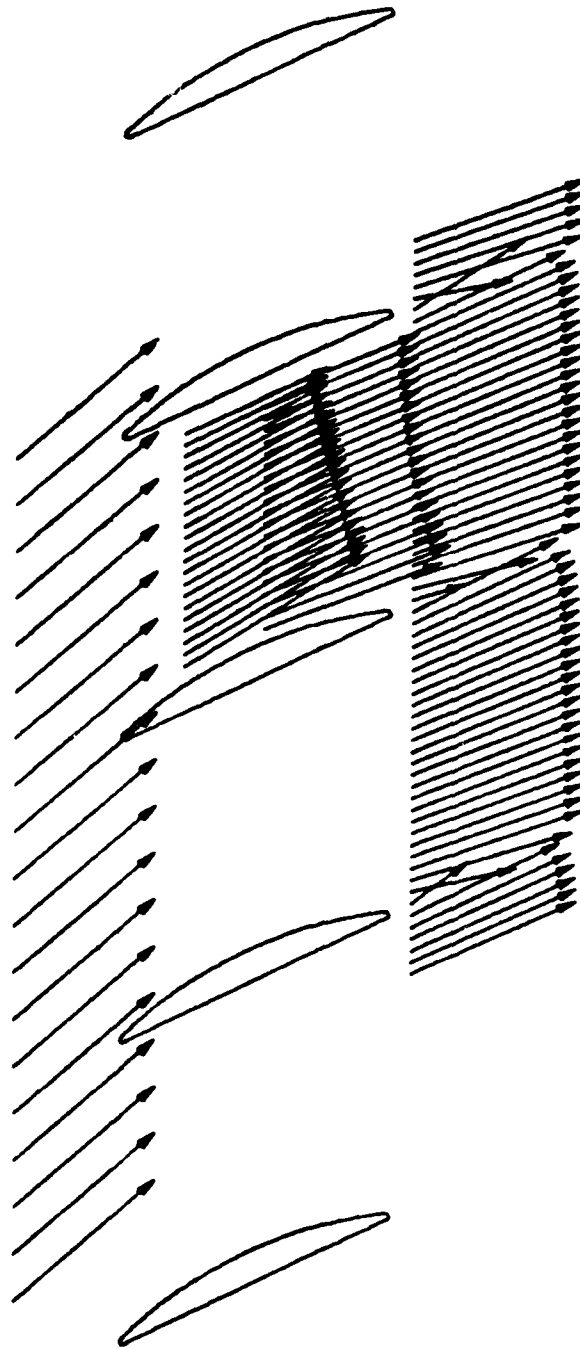


Figure 12. Measured Velocities in Blade Passage Region

TEST NOS. CT33, BB03, BB06
STAGGER ANGLE: 25.0
ANGLE OF ATTACK: 20.0
INLET VELOCITY: 159.8 FT/SEC
REYNOLDS NUMBER: 200569



Figure 13. Measured Velocities in Blade Passage Region

TEST NOS. CT28, BB01, BB07
STAGGER ANGLE: 25.0
ANGLE OF ATTACK: 25.0
INLET VELOCITY: 159.7 FT/SEC
REYNOLDS NUMBER: 199262

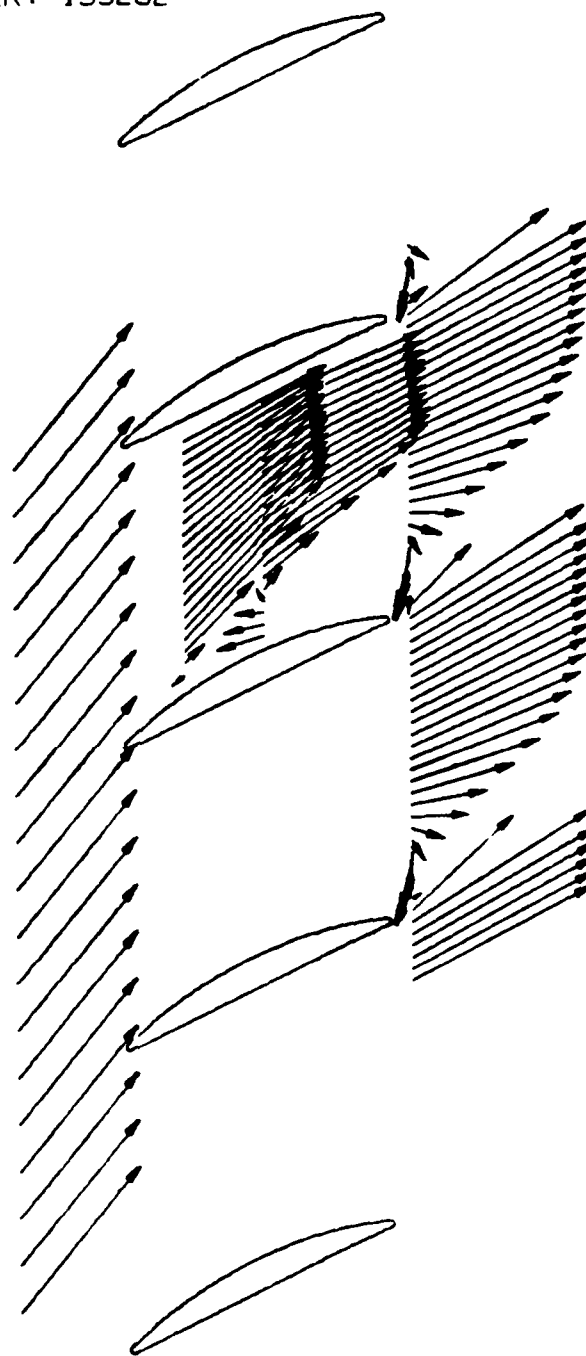


Figure 14. Measured Velocities in Blade Passage Region

TEST NOS. CT27, BB02, BB08
STAGGER ANGLE: 25.0
ANGLE OF ATTACK: 30.0
INLET VELOCITY: 157.1 FT/SEC
REYNOLDS NUMBER: 196525

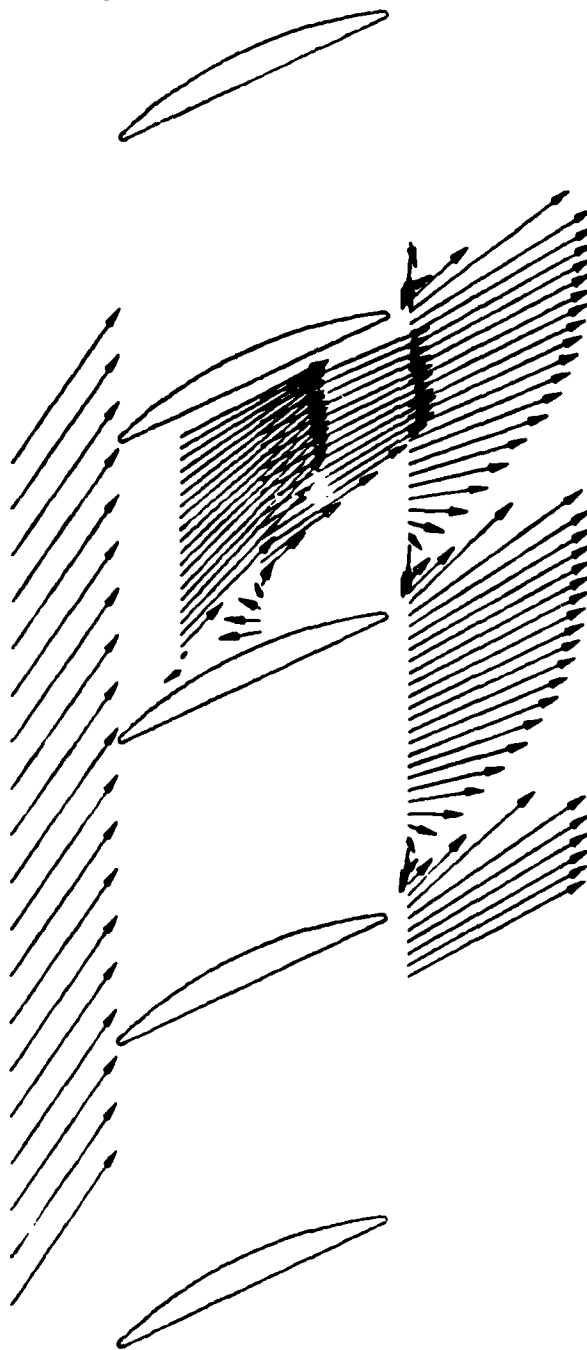


Figure 15. Measured Velocities in Blade Passage Region

TEST NOS. CT04, BB09, BB13
STAGGER ANGLE: 36.5
ANGLE OF ATTACK: 15.0
INLET VELOCITY: 157.5 FT/SEC
REYNOLDS NUMBER: 199985



Figure 16. Measured Velocities in Blade Passage Region

TEST NOS. CT06. BB10. BB14
STAGGER ANGLE: 36.5
ANGLE OF ATTACK: 20.0
INLET VELOCITY: 158.7 FT/SEC
REYNOLDS NUMBER: 200316

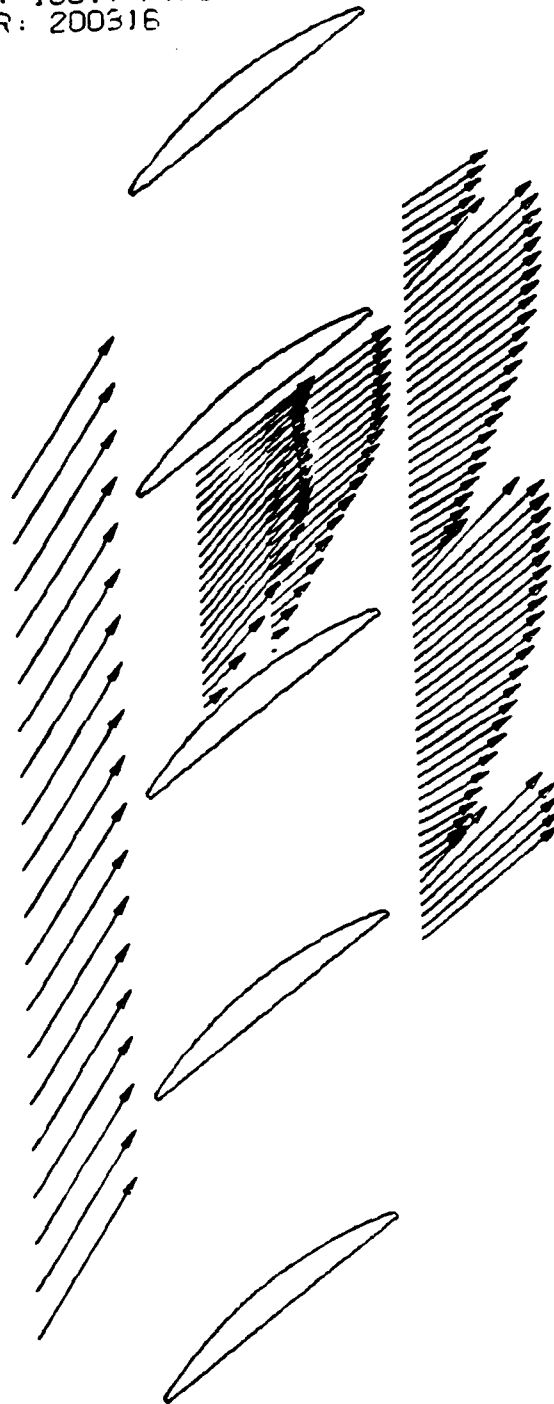


Figure 17. Measured Velocities in Blade Passage Region

TEST NOS. CT01, BB11, BB15
STAGGER ANGLE: 36.5
ANGLE OF ATTACK: 25.0
INLET VELOCITY: 155.9 FT/SEC
REYNOLDS NUMBER: 199865

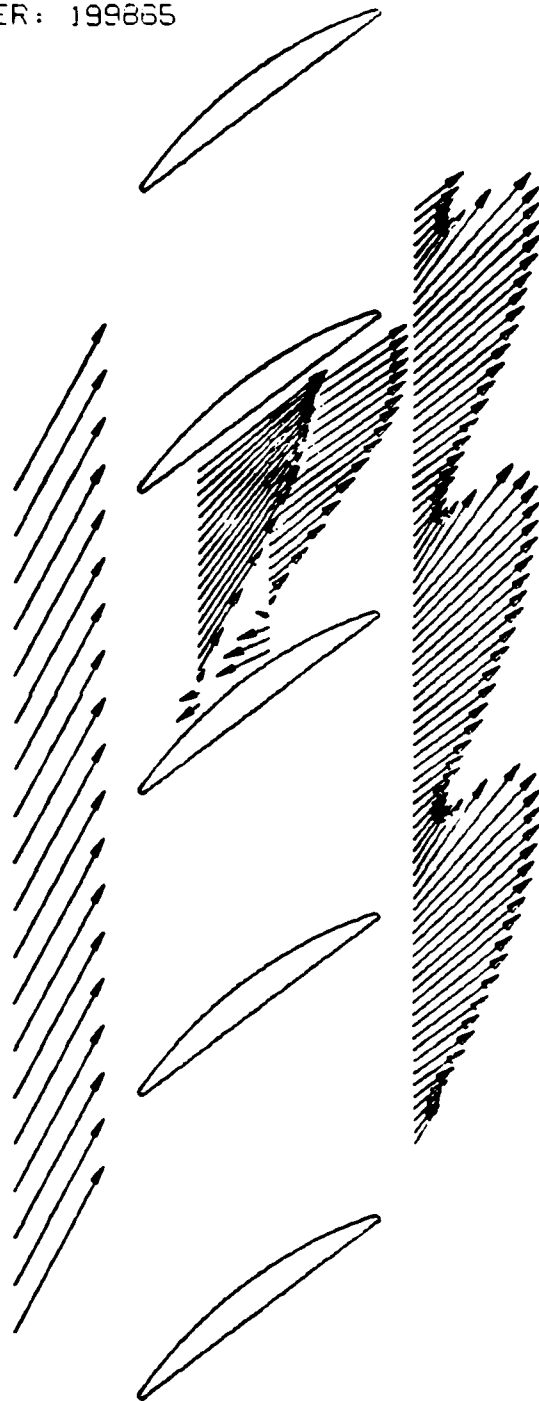


Figure 18. Measured Velocities in Blade Passage Region

TEST NOS. CT10, BB12, BB16
STAGGER ANGLE: 36.5
ANGLE OF ATTACK: 30.0
INLET VELOCITY: 154.9 FT/SEC
REYNOLDS NUMBER: 200647

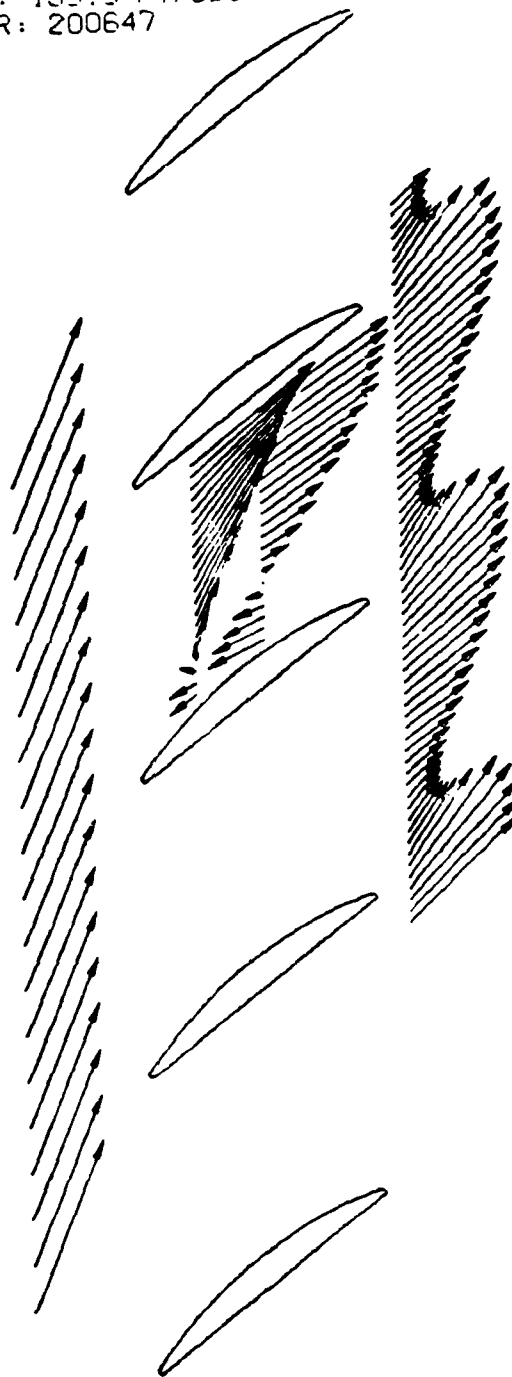


Figure 19. Measured Velocities in Blade Passage Region

TEST NOS. CT39, BB17, BB21
STAGGER ANGLE: 45.0
ANGLE OF ATTACK: 15.0
INLET VELOCITY: 158.2 FT/SEC
REYNOLDS NUMBER: 200929



Figure 20. Measured Velocities in Blade Passage Region

TEST NOS. CT37, BB18, BB22
STAGGER ANGLE: 45.0
ANGLE OF ATTACK: 20.0
INLET VELOCITY: 159.4 FT/SEC
REYNOLDS NUMBER: 200049

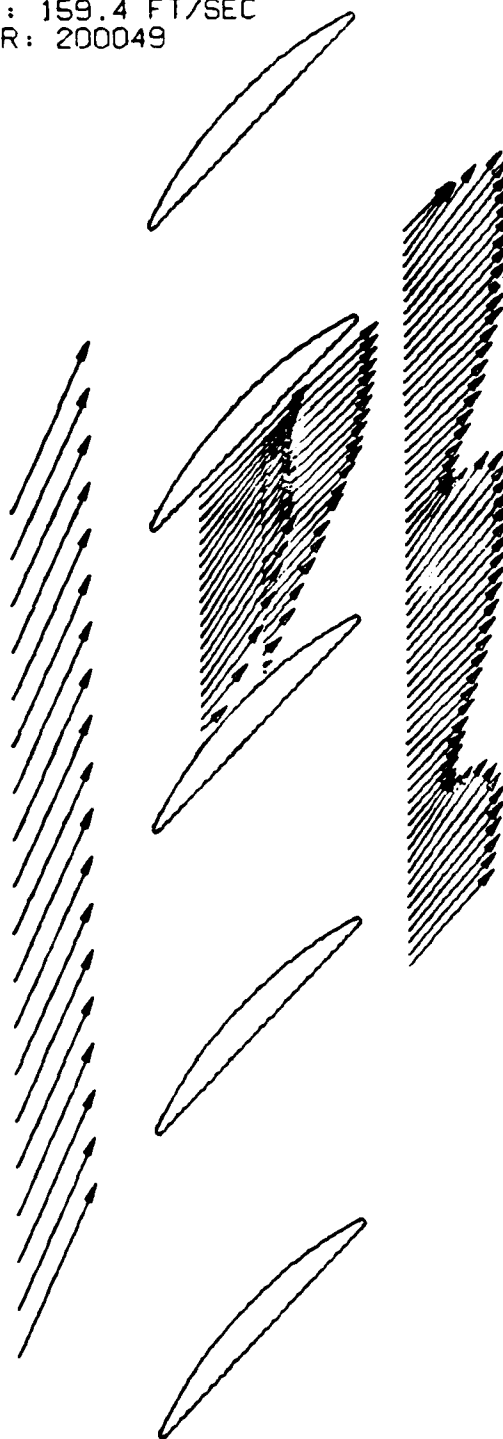


Figure 21. Measured Velocities in Blade Passage Region

TEST NOS. CT41, BB19, BB23
STAGGER ANGLE: 45.0
ANGLE OF ATTACK: 25.0
INLET VELOCITY: 159.1 FT/SEC
REYNOLDS NUMBER: 200829

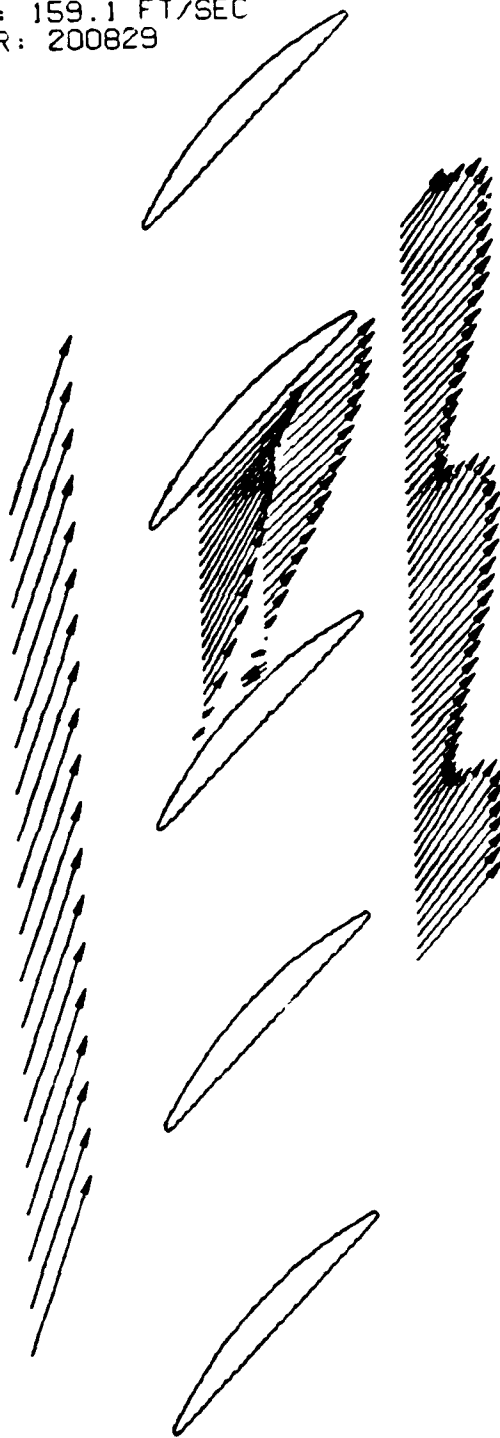


Figure 22. Measured Velocities in Blade Passage Region

TEST NOS. CT42, BB20, BB24
STAGGER ANGLE: 45.0
ANGLE OF ATTACK: 30.0
INLET VELOCITY: 159.2 FT/SEC
REYNOLDS NUMBER: 199800

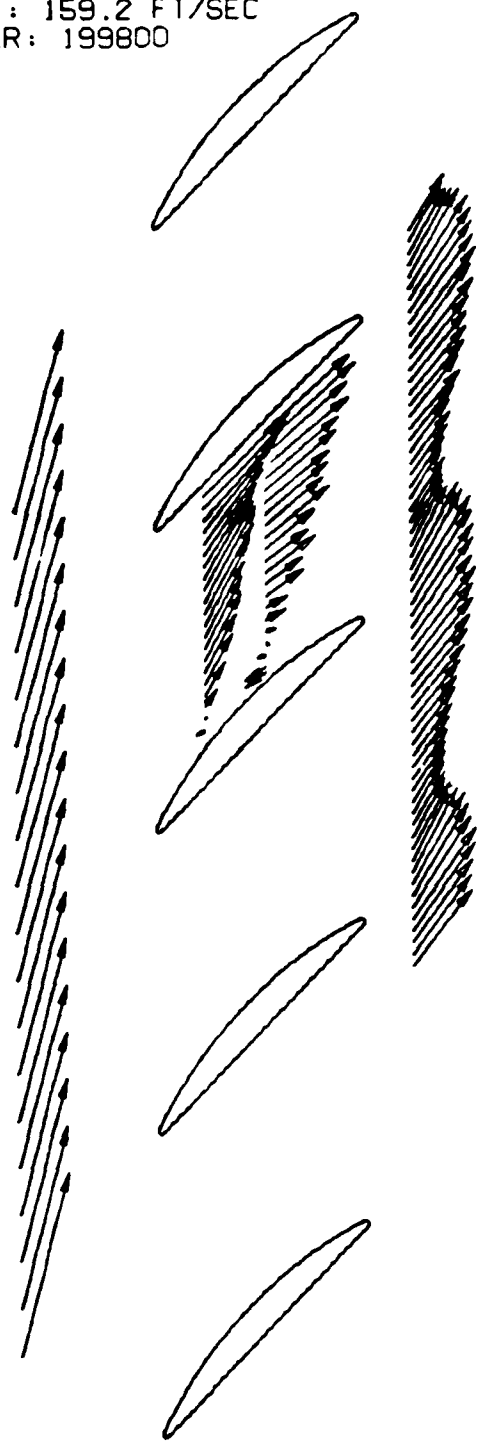


Figure 23. Measured Velocities in Blade Passage Region

passage. The flow outside of the reverse flow region has a fairly linear velocity profile with a slight increase in velocity going from the pressure surface toward the separated region. This increase in velocity indicates that some of the potential flow nature of the flow still exists outside of the separated region. For this stagger of 25 degrees, the flow is seen to have characteristics of a jet of potential flow and a viscous separated region.

Comparing Figs. 14, 18, and 22, which are for an angle of attack of 25 degrees, and Figs. 15, 19, and 23, which are for an angle of attack of 30 degrees, it is seen for the two cascades with the larger staggers that two distinct regions of the flow are not as apparent as they are for the 25 degree stagger cascade. For the cascades with staggers of 36.5 and 45 degrees, nearly all or all of the passage is affected by the viscous effects of the shear flow surrounding the separated region. It is noted that the greater blockage seen to occur for the higher staggered cascades is consistent with the occurrence of propagating stall observed for the cascades with $\xi = 36.5$ and 45 degrees, but not observed for the 25 degree stagger cascade.

Results from a numerical simulation of the flow through a cascade of flat plate airfoils were used to further illustrate the effects of blade stagger and to define the correct limits for the cascade performance as an inlet angle of 90 degrees is approached. The flow simulation was obtained by numerically solving the two-dimensional, steady, constant viscosity, incompressible Navier-Stokes equation using the SIMPLER algorithm of Patankar.

The velocity vector profiles obtained from the numerical results

have the same general shapes and exhibit the same trends with respect to stagger as do the measured velocity profiles. Figure 24 shows a sample comparison of the numerically-predicted velocity field with the measured values, for an angle of attack of 30 degrees. The obvious reasons for the differences in the absolute values of the velocities are the approximations and simplifying assumptions made in the numerical prediction. Even at an angle of attack of 15 degrees, the numerical results indicate some reverse flow. This separation is most likely the result of the sharp leading edge associated with approximating the blades as flat plates. The extent of the reverse flow is predicted by the analysis to be larger for the higher stagger angles. This result is consistent with the observation from the surface flow visualization that full stall occurs at a slightly lower angle of attack for cascades with greater stagger.

For the larger angles of attack, the velocity of the reverse flow predicted numerically was found to have greater magnitude, but with the region of the separated flow extending a smaller distance into the passage than the corresponding measured flow. This difference is thought to be due primarily to the curvature of the suction surface of the real blade rather than due to the finite thickness of the real blade. Full details of the velocity measurements and theory development are provided in Ref. 5.

3.1.9 Cascade Pressure Measurements

Figure 25 shows an example of total pressure and static pressure losses measured behind the 25 degree stagger cascade, for a very high

angle of attack of 45 degrees. Predictions of the previously-mentioned theory are shown for comparison. At this angle of attack, total pressure losses are extremely high, and extend over a large percentage of the cascade pitch. Large static pressure variations are measured. Agreement between theory and experiment is good for the lower loss regions, but the theory significantly under-predicts the high levels of static and total pressure coefficient. Much better agreement is obtained for lower angles of attack. Complete measurements and comparisons are presented in Ref. 5.

Pressure measurements were made employing static taps on the suction and pressure surfaces of the cascade blades. The taps were located at mid-span, and in the centermost blade passage. Measured and predicted pressure coefficients are shown in Fig. 26, for the same flow conditions shown in Fig. 25. Here, agreement is excellent, especially considering the extremely high angle of attack of the flow.

3.1.10 Cascade Performance

The ultimate goal of the cascade measurement program was to provide improved understanding of the cascade stalling process, and to provide measurements of the fluid dynamic losses of the cascade at high angle of attack for three stagger angles. The previously-described measurements were utilized to compute the cascade losses with results shown in Fig. 27. The loss parameter ω_2 is the mass-averaged total pressure loss coefficient immediately behind the cascade, referenced to the mean velocity entering the cascade.

A principal feature of the loss behavior is the lower rate-of-rise

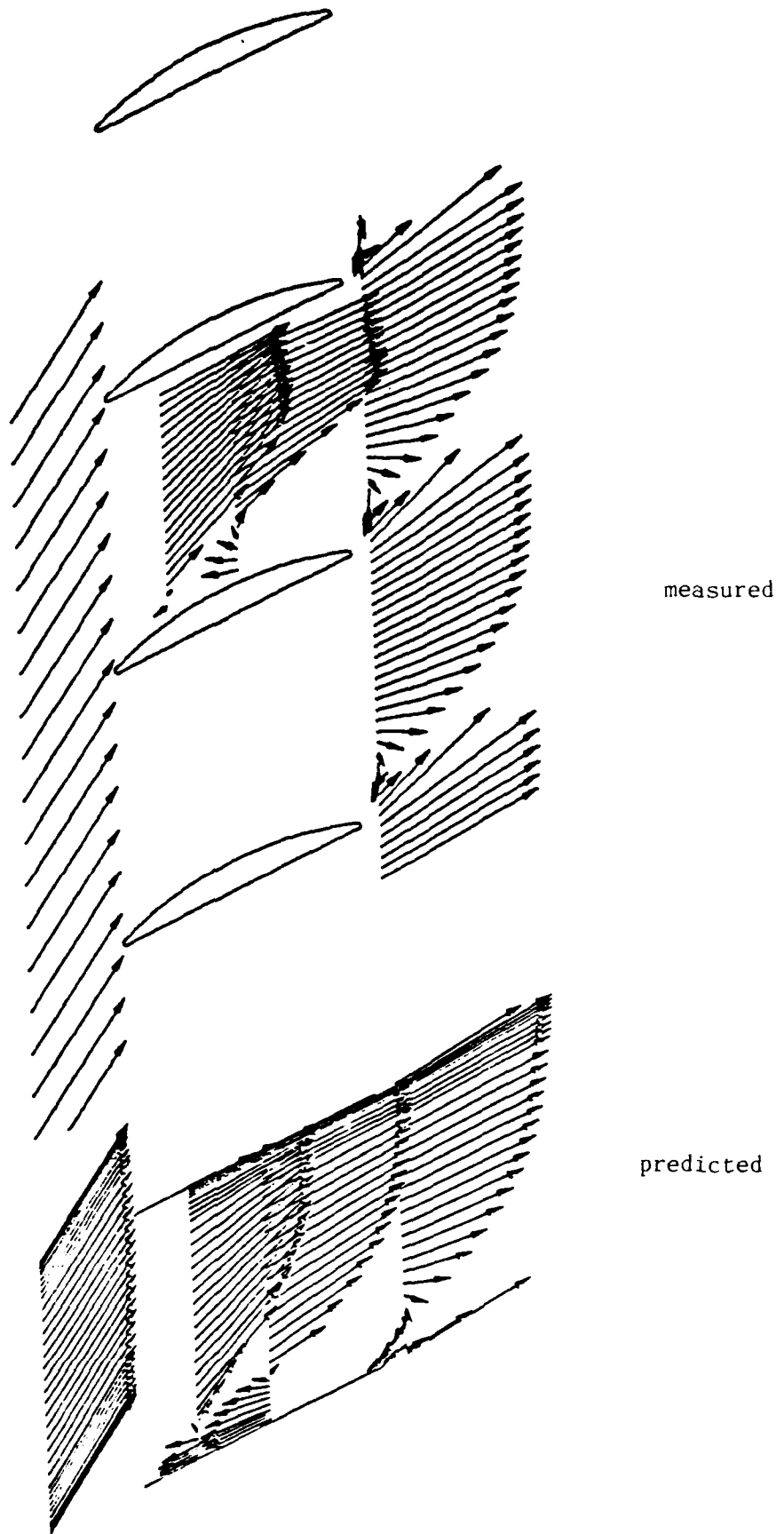
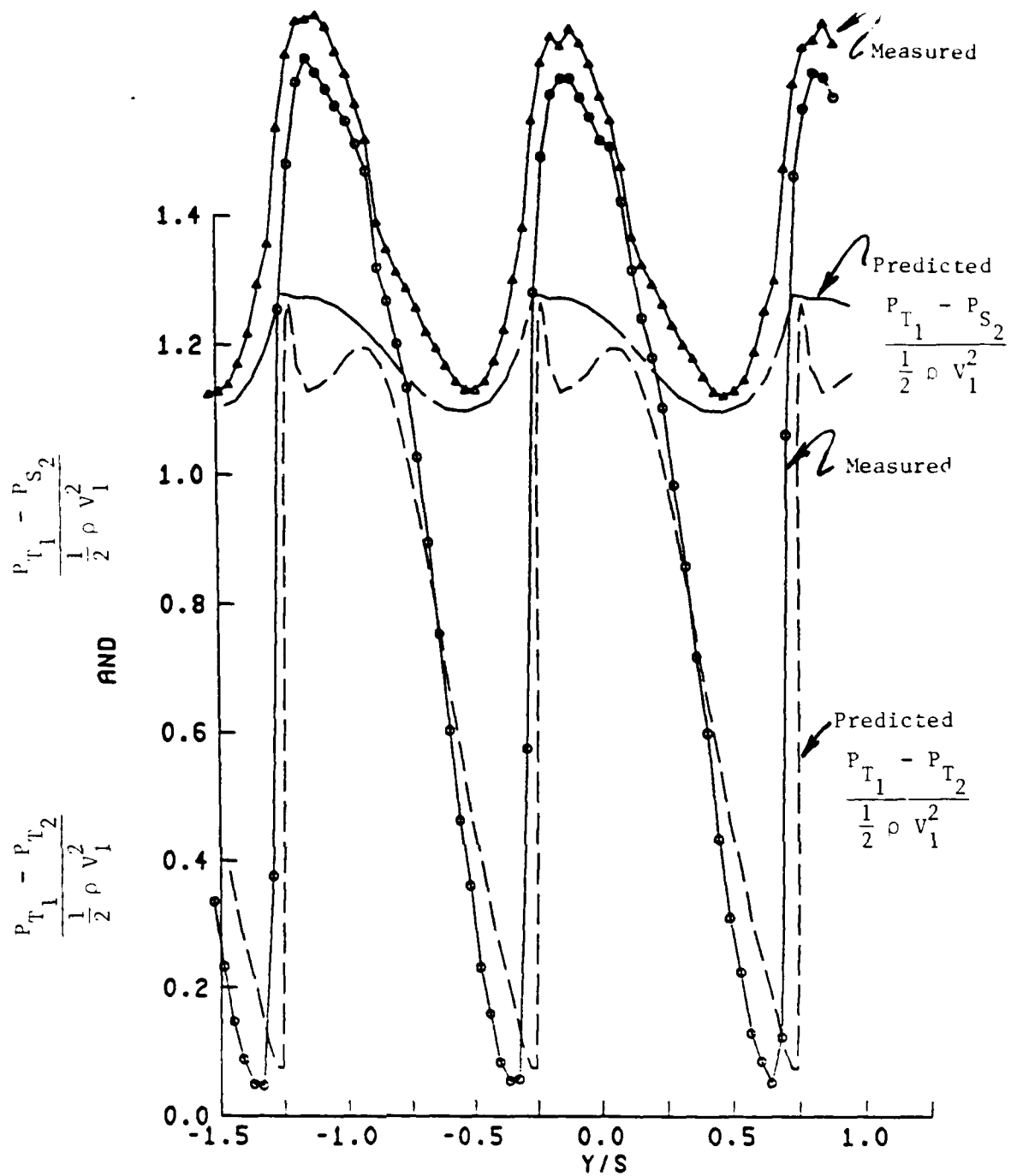
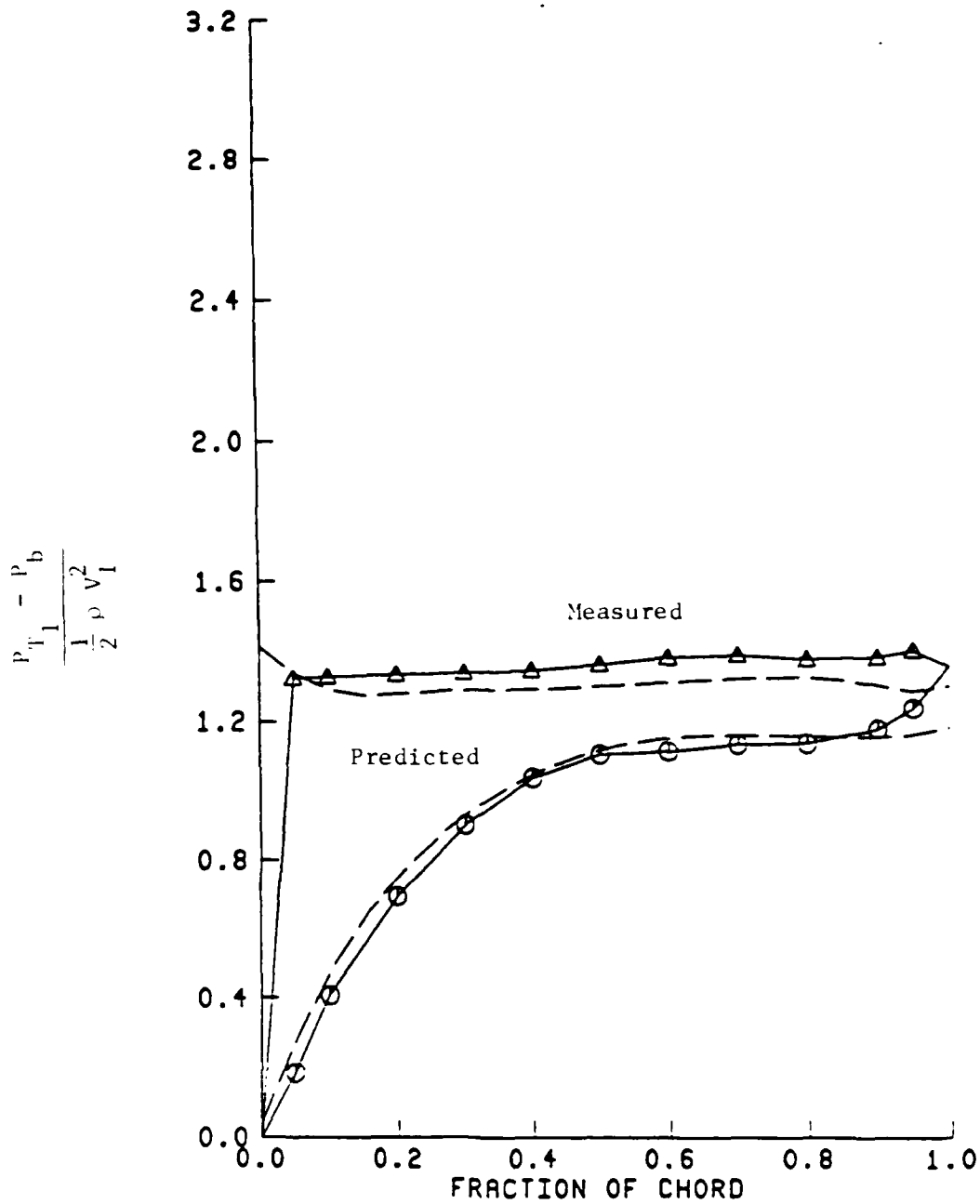


Figure 24. Comparison of Measured and Calculated Velocities in Blade Passage Region; $\xi = 25^\circ$, $\alpha = 30^\circ$



TEST NUMBERS: CT24, PT14
 STAGGER ANGLE: 25.0
 ANGLE OF ATTACK: 45.0
 INLET VELOCITY: 158.2 FT/SEC
 REYNOLDS NUMBER: 197888

Figure 25. Measured and Predicted Cascade Losses



TEST NUMBERS: CT24, PT14
 STAGGER ANGLE: 25.0
 ANGLE OF ATTACK: 45.0
 INLET VELOCITY: 158.2 FT/SEC
 REYNOLDS NUMBER: 197888

Figure 26. Measured and Predicted Cascade Pressures

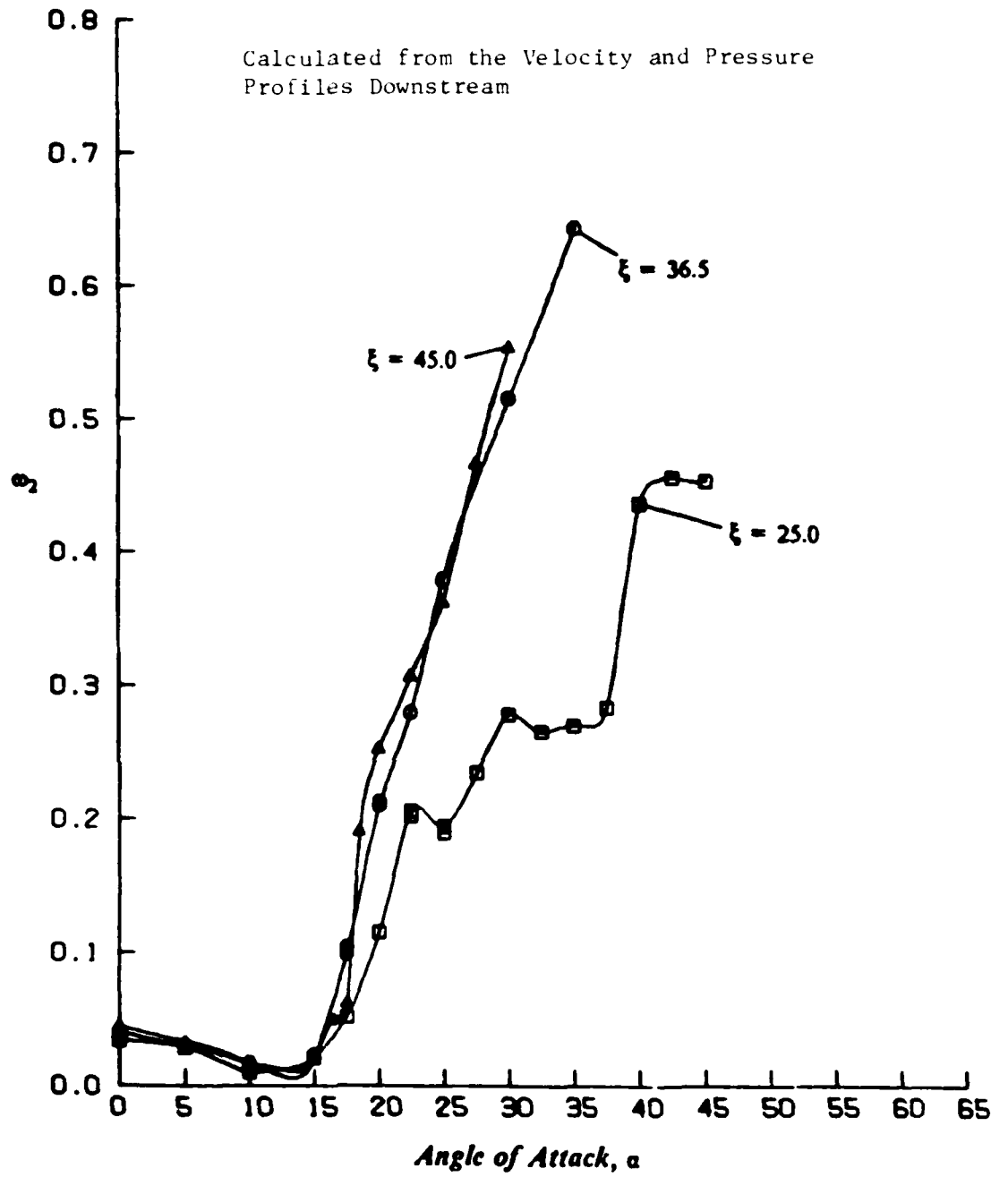


Figure 27. Flow Losses for Three Stagger Angles

of the losses for 25 degrees stagger, as compared with that for the 36.5 and 45 degree stagger cases. This result is assumed to be due to the observed differences in cascade blockage for the three stagger angles, as previously discussed. The results are very important with regard to the model for rotating stall, which has been found to be primarily influenced by the slope of the loss curve after stalling has occurred.

The blade normal force coefficient was calculated from the measured velocity and pressure profiles, with the result shown in Fig. 28. Again, a significant difference is noted for the 25 degree stagger angle results.

Loss and normal force coefficient predictions of the mathematical model are shown in Figs. 29 and 30. Trends are correctly predicted, but differences between 36.5 and 45 degree stagger angle predictions are larger than experimentally observed. Reasons for the differences are being assessed.

3.1.11 Conclusions, Cascade Measurements

Extensive measurements of cascade flow characteristics and performance were accomplished. Results were obtained for three stagger angles, as planned. Significant effects of stagger angle were noted, which are expected to influence predictions of the post-stall compressor stage model. Supporting flow visualizations provided new insight into the cascade stalling process. The data obtained were compared with predictions of a mathematical model developed under the program, with good results. For future use, all data obtained are reported in Refs. 3, 4, and 5.

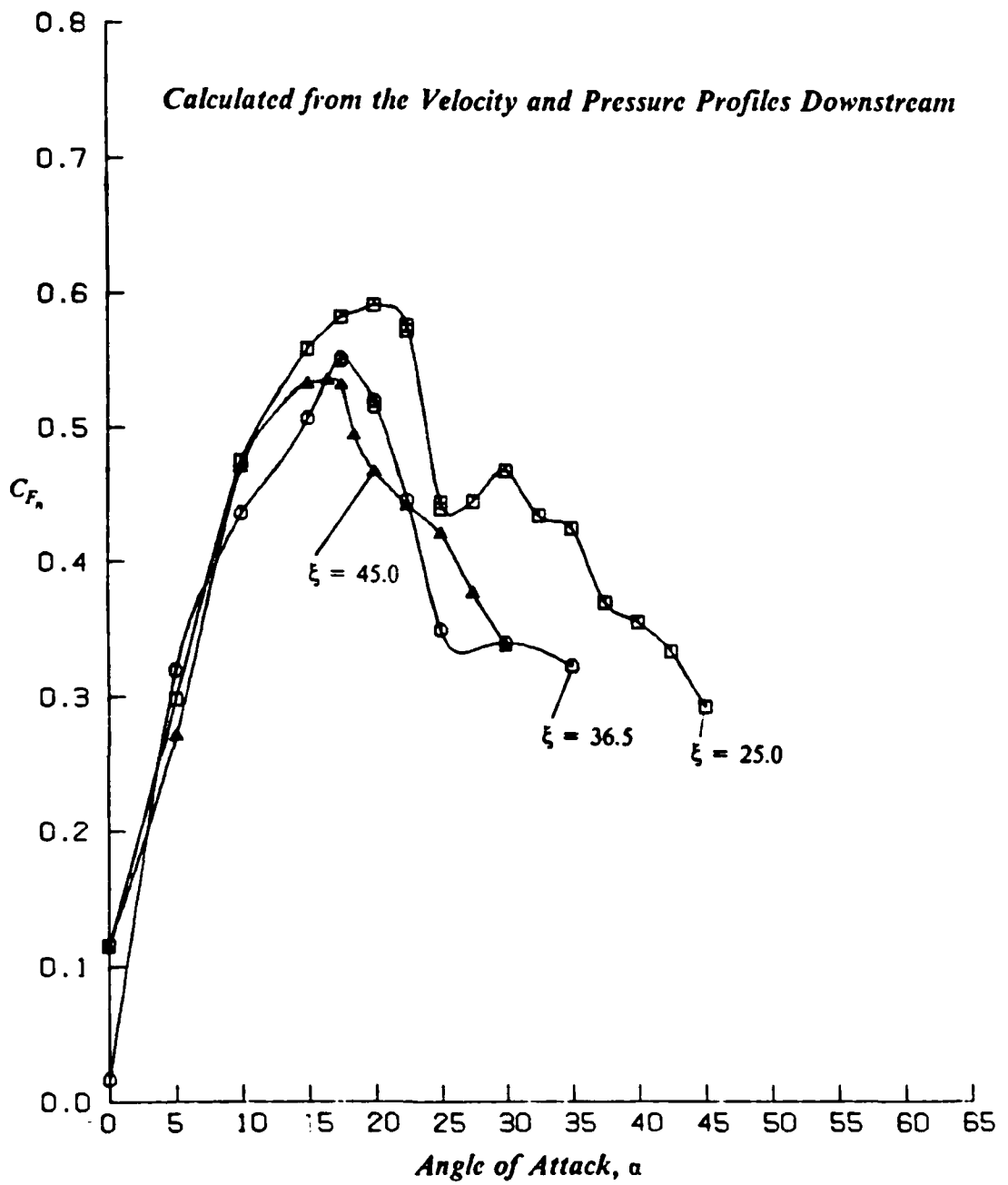


Figure 28. Normal Force Coefficient for Cascade Blade from Measurements

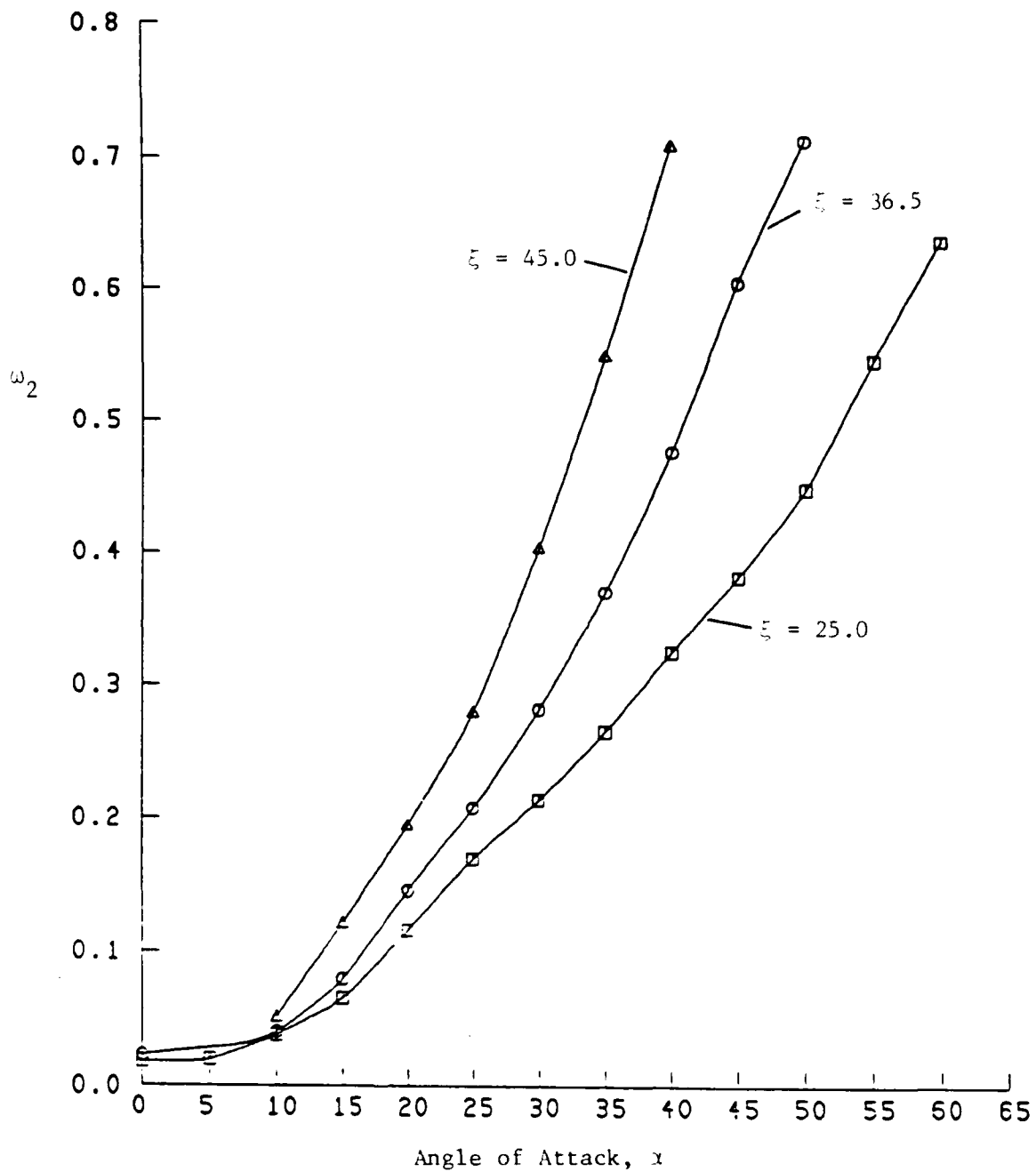


Figure 29. Mass Average Total Pressure Loss Evaluated From the Numerical Results for $Re = 200,000$

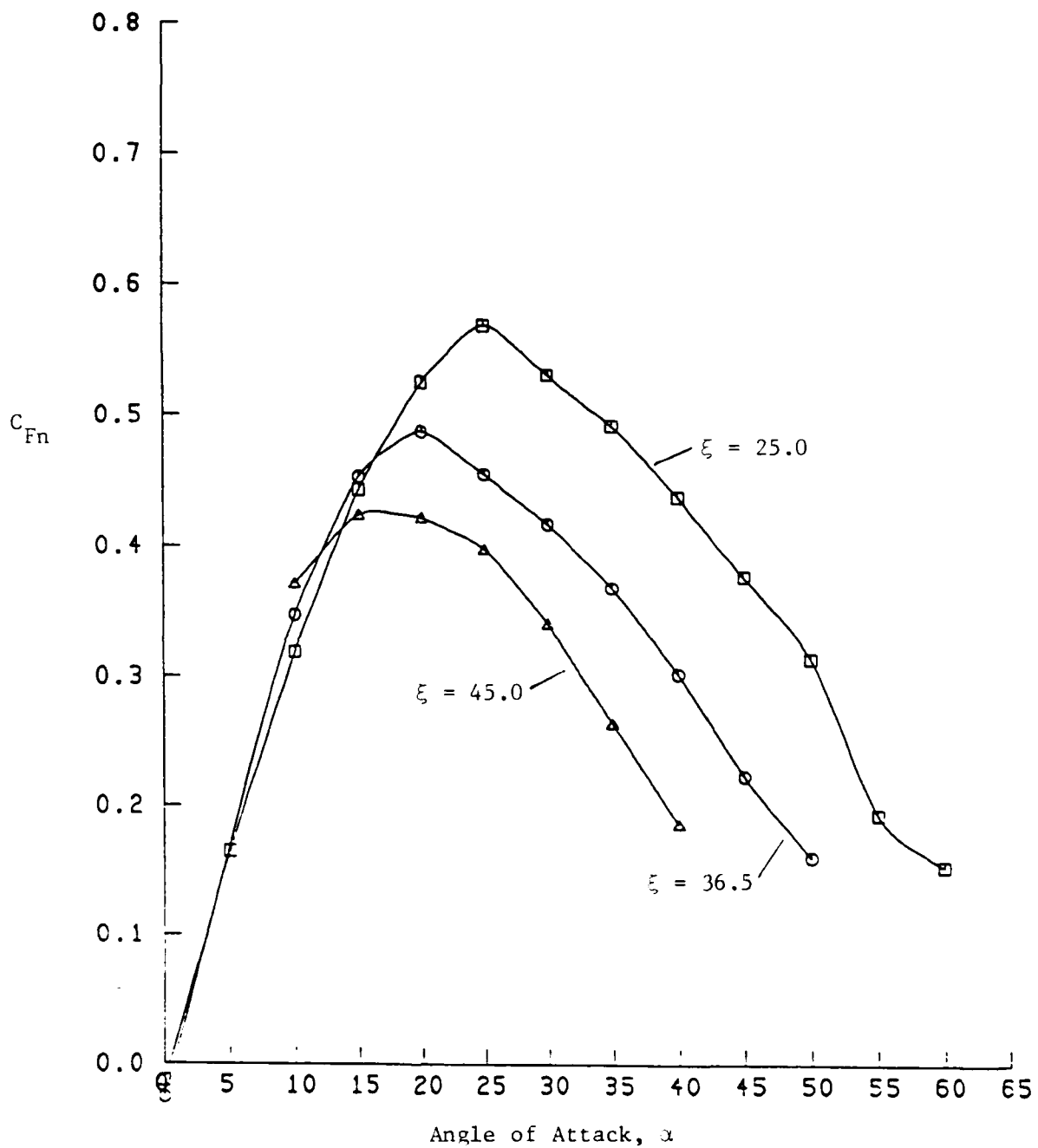


Figure 30. Calculated Normal Force Coefficient for Cascade Blade

3.2 Prediction of Separated Flow in Cascades

A mathematical model for prediction of separated flows in cascades was developed under the program. As previously noted, the flow simulation was obtained by numerically solving the two-dimensional, steady, constant, viscosity, incompressible Navier-Stokes equations using the SIMPLER algorithm of Patankar. Comparisons of the theory predictions and measured results were shown in the previous sections. The complete development of the theory is given in Ref. 5.

3.3 Improvements in Post-Stall Compressor Stage Model

At the beginning of the program, a post-stall predictive model existed from previous work¹, but improvements in the model were desirable. A description of the model and progress made was published⁶, and a copy of the paper is included here as Appendix A. As a result of work under the present program, the model is presently capable of predicting a compressor stage post-stall characteristic, and accomodates a non-uniform downstream pressure boundary behind the simulated rotor. Work continues to add a stator row to the model, thus simulating a full stage. With the model and the data obtained from the investigation, new insights have been provided, and work continues to add to the understanding of the mechanisms of compressor post-stall behavior.

4.0 PUBLICATIONS

1. Cousins, W. T., and W. F. O'Brien, "Compressor Stage Post-Stall Analysis," AIAA Paper No. 75-1349.

When the addition of a downstream stator row model is complete, it is planned to submit a revised version of this paper to the AIAA Journal of Propulsion and Power.

2. The following paper has been submitted for presentation and publication at the 1988 ASME Gas Turbine Conference.

**Separated Flow in a Compressor Cascade - Part I:
Flow Visualization and Time-Mean Velocity Measurements**

by

Adam M. Yocum, II
Research Associate, Applied Research Laboratory
The Pennsylvania State University
State College, PA

and

Walter F. O'Brien
Professor of Mechanical Engineering
Virginia Polytechnic Institute and State University
Blacksburg, VA

ABSTRACT

This study was conducted for the purposes of providing a more fundamental understanding of the flow and to provide performance data for fully stalled cascades. Performance data for fully stalled compressor blade rows are required to model compressor stall phenomena using currently available techniques. Cascades of a single blade geometry and a solidity of unity were studied for three stagger angles and over the full range of angle of attack extending well into the stalled flow regime. The Reynolds number was also varied for a limited number of cases.

Part I of this paper presents the results obtained from surface flow visualization tests, smoke flow visualization tests, and time-mean velocity measurements. Surface flow visualization studies using the oil-film visualization technique were conducted to examine the two-dimensionality of the flow and to determine the location of the

separation line on the blades. Smoke flow visualization studies were conducted for determining the existence and type of unsteadiness. The visualized flow was filmed at a rate of 4000 frames per second using a rotating prism high speed motion picture camera, and was subsequently studied in detail by examining the films at a normal projection speed of 16 frames per second. The surface flow visualization and the smoke flow visualization showed that the blade stagger angle is a key parameter in determining the location of the separation line and the occurrence of propagating stall. Time mean velocity measurements obtained with a dual hot split film probe also showed that the separated velocity profiles within the blade passages and the downstream profiles in the wake have distinctly different characteristics depending on the stagger angle. The characteristics of the velocity profiles can be related by physically reasoning to the occurrence of propagating stall and the performance of the fully stalled cascade, which is presented in Part II of this paper.

**Separated Flow in a Compressor Cascade - Part II:
Cascade Performance**

ABSTRACT

This study was conducted for the purposes of providing a more fundamental understanding of the flow and to provide performance data for fully stalled cascades. Performance data for fully stalled compressor blade rows are required to model compressor stall phenomena using currently available techniques. Cascades of a single blade geometry and a solidity of unity were studied experimentally for three

stagger angles and over the full range of angle of attack extending well into the stall flow regime. The Reynolds number was also varied for a limited number of cases.

Part II of this paper presents the results from the velocity and pressure measurements made in the cascade and the overall cascade performance evaluated from these measurements. In addition, results from a numerical simulation of the flow through a cascade of flat plate airfoils is used to further illustrate the effects of blade stagger and to define the correct limits for the cascade performance as an inlet angle of 90 degrees is approached. The flow simulation was obtained by numerically solving the two-dimensional, steady, constant viscosity, incompressible Navier-Stokes equations using the SIMPLER algorithm of Patankar. The cascade performance is presented in terms of the normal force coefficient and the mass averaged total pressure loss through the cascade as a function of angle of attack. The results indicate that the slope of the total pressure loss curve for the flow immediately downstream of the cascade is steeper for cascades with greater stagger, and the losses continue to rise as the limiting case of 90 degree inlet flow is approached. The losses calculated for the flow when it becomes fully mixed are not as greatly influenced by stagger. The normal force coefficient was found to increase to a peak value near the angle of attack where full leading stall first occurs. A further increase in angle of attack results in a decline in the normal force coefficient. The peak value of the normal force coefficient is greater and occurs at a higher angle of attack for the cascades with greater stagger.

5.0 GRADUATE STUDENTS PARTICIPATING IN THE PROGRAM

1. Donald R. Piat, M.S., 1986
2. Thomas W. Russ, M.S., 1987
3. Adam M. Yocum, Ph.D., expected 1987
4. William T. Cousins, Ph.D., expected 1987

6.0 INTERACTIONS AS A PART OF THE PROGRAM

1. Pratt and Whitney Co., West Palm Beach, Florida; visits and discussion of development of stage model; supply of high-angle-of-attack loss data.
2. Garrett Turbine Engine Company, Phoenix, Arizona; detailed search of available high-angle-of-attack loss data; technical presentation.
3. Wright-Patterson Air Force Base, Ohio; presentation of results of stage modeling and cascade tests; consultation on compressor stall tests.
4. Arnold Engineering Development Center, Tennessee; communication and consultation on development of multistage compressor models using research results of the present program.

7.0 REFERENCES

1. Sexton, M. R., and W. F. O'Brien, "A Model for Dynamic Loss Response in Axial Flow Compressor," ASME Paper No. 81-GT-154, March 1981.
2. O'Brien, W. F., H. L. Moses, S. B. Thomason, and A. M. Yocum, "High Angle-of-Attack Cascade Measurements and Analysis," Proceedings of the 6th International Symposium of Air Breathing Engines, Paris, France, June 1983.
3. Russ, T. W., "A Surface Flow Visualization Study of Boundary Layer Behavior on the Blades of a Solid-Wall Compressor Cascade at High Angles of Attack," Master of Science Thesis, Mechanical Engineering Department, Virginia Polytechnic Institute and State University, Blacksburg, VA, January 1987.

4. Piatt, D. R., "Development of a Geometric Model for the Study of Propagating Stall Inception Based on Flow Visualization in a Linear Cascade," Master of Science Thesis, Mechanical Engineering Department, Virginia Polytechnic Institute and State University, Blacksburg, VA, July 1986.
5. Yocum, A. M., "Separated Flow in a Compressor Cascade," Ph.D. Dissertation, Department of Mechanical Engineering, Virginia Polytechnic Institute and State University, Blacksburg, VA, expected October 1987.
6. Cousins, W. T., and W. F. O'Brien, "Axial-Flow Compressor Stage Post Stall Analysis, AIAA-85-1349, July 1985.

AIAA'85

AIAA-85-1349

**Axial - Flow Compressor Stage
Post - Stall Analysis**

W.T. Cousins, Garrett Turbine Engine Co.,
Phoenix, AZ; and W.F. O'Brien,
Virginia Polytechnic Institute and
State University, Blacksburg, VA

**AIAA/SAE/ASME/ASEE 21st Joint
Propulsion Conference**

July 8-10, 1985 / Monterey California

AXIAL-FLOW COMPRESSOR STAGE POST-STALL ANALYSIS

W. T. Cousins*
Garrett Turbine Engine Company
Phoenix, AZ 85010

W. F. O'Brien**
Mechanical Engineering Department
Virginia Polytechnic Institute and State University
Blacksburg, VA 24061

Abstract

Rotating stall in a compressor stage is simulated by the numerical solution of a fluid dynamic model of an inlet guide vane and rotor row. The mathematical formulation of the model is described. Solutions for the flow upstream and downstream of the modeled stage are obtained for normal unstalled operation and for a simulation of stable rotating stall. Examples of the predicted velocity and pressure fields are shown, and conclusions are developed regarding recovery from rotating stall. The influence of the rotor row loss coefficient curve and other blade row design variables on model predictions are studied.

Nomenclature

BV blade velocity
C absolute velocity
F Fourier Transform
 F^{-1} Inverse Fourier Transform
H mechanical energy per unit mass (fluid head)
 l blade chord length
P static pressure
 P_0 total pressure
Q volume flow rate
 s blade pitch
 t time
TF transfer function
U steady axial velocity
 u axial perturbation velocity
 \bar{u} $U + u$
V steady tangential velocity
 v tangential perturbation velocity
 \bar{v} $V + v$
w relative velocity

x axial coordinate
y tangential coordinate
 ζ vorticity
 ξ blade stagger angle (ref. axial direction)
 ρ density
 ϕ potential function
 $\bar{\phi}$ flow coefficient
 ω total pressure loss coefficient
 τ time constant
 ψ stream function
 $\bar{\psi}$ pressure coefficient

SUBSCRIPTS

1 conditions upstream of rotor
2 conditions downstream of rotor

Introduction

Axial-flow compressor post-stall behavior is an important aspect of aircraft engine stability and operability. The rotating stall phenomenon, which can occur under certain conditions, limits the range of engine operation. Reduced compressor pressure rise and mass flow associated with rotating stall cause performance loss and engine overtemperature, and locally unsteady flow within the compressor blading can produce damage through aeromechanical effects. Compressor recovery from the globally-stable rotating stall condition is an important concern.

Conditions which give rise to rotating stall and aspects of compressor behavior in rotating stall have been discussed by several authors^{1,2,3}. Analyses by Moore⁴ have shown the effect of the general shape of the compressor characteristic on post-stall and recovery behavior. The present work provides predictions of compressor stage post-stall behavior from a flow model which includes blade row design features and aerodynamics. The model, based on an approach originally developed by Takata and Nagano⁵, shows local features of rotating stall in a compressor stage, including flow velocities and pressures.

* Aerothermo. Design Engineer, Garrett Turbine Engine Company Phoenix, Arizona; Member AIAA

** Professor of Mechanical Engineering; Member AIAA

Stall inception and recovery points, and a post-stall operating characteristic are predicted. The details of the loss behavior of the rotor blade row are found to have the principal influence on model predictions.

The Model

The numerical model represents components of an axial-flow compressor, that is, a set of inlet guide vanes and a rotor. In the model, the compressor rotor is represented by a discontinuity surface (a semi-actuator disk) at which the energy transfer due to the rotor blades is introduced into the flow. The flow fields upstream and downstream of the rotor are interactively coupled using the semi-actuator disk. The model is used to predict whether the onset of rotating stall will occur under any particular set of operating conditions by imposing a perturbation upon the uniform flow field of the upstream face of the rotor semi-actuator disk. If the rotor is operating in a stable regime, the perturbation velocity will diminish with time and the flow will return to its former uniform condition. If the rotor flow is made unstable, the disturbance will grow into a fully-developed pattern which will propagate around the rotor semi-actuator disk in the form of a rotating stall.

The solution of the analytical model is carried out using numerical techniques to solve the unsteady, nonlinear equations which represent the flow fields and the characteristics of the semi-actuator disk.

The flow fields upstream and downstream of the rotor are represented by two-dimensional flow models. These flow fields are obtained by unrolling a unit thickness cylindrical section of the compressor annulus into a two-dimensional plane, as shown in Fig. 1. The upstream flow is assumed to be incompressible, inviscid, and irrotational. The downstream flow is considered incompressible, inviscid, and rotational.

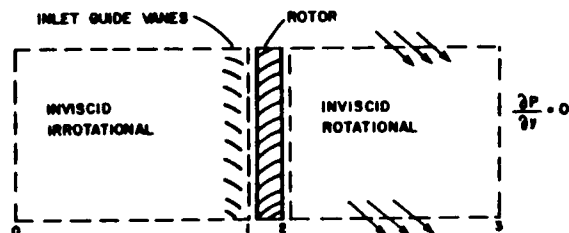


Fig. 1 Model Flowfield for Single Stage Compressor

In models of this type, one must be able to calculate the dynamic manner in which the blade row characteristics respond to changes in the inlet flow. The present stall model improves on the first-order techniques many investigators have used in the past by incorporating an improved dynamic loss model developed by Sexton.⁶ The model utilizes experimentally-measured blade forces to describe the dynamic blade row characteristics. The dynamic loss for each time step in the numerical calculation is determined by first calculating the quasi-steady variation in total

pressure loss along the semi-actuator disk representing the compressor rotor, employing the quasi-steady loss curve and the flow exit angle for the rotor cascade. A dynamic response expression in the form of a transfer function (TF) is then used to compute the dynamic loss.

The Rotor Semi-Actuator Disk

The flow upstream of the rotor semi-actuator disk is assumed to consist of a uniform velocity field on which a perturbation velocity can be superimposed. Neglecting body forces, the momentum equations for the perturbation flow field take the form of the Euler Equations,

$$\frac{\partial u}{\partial t} = -\frac{1}{\rho} \frac{\partial P}{\partial x} - u \frac{\partial u}{\partial x} - v \frac{\partial u}{\partial y} \quad (1)$$

$$\frac{\partial v}{\partial t} = -\frac{1}{\rho} \frac{\partial P}{\partial y} - u \frac{\partial v}{\partial x} - v \frac{\partial v}{\partial y} \quad (2)$$

The total fluid mechanical energy per unit mass is

$$H \equiv \frac{P}{\rho} = \frac{1}{\rho} P + \frac{1}{2} (u^2 + v^2) \quad (3)$$

Taking the partial derivative with respect to the x and y directions yields for the perturbation flow field

$$\frac{\partial H}{\partial x} = \frac{1}{\rho} \frac{\partial P}{\partial x} + u \frac{\partial u}{\partial x} + v \frac{\partial v}{\partial x} \quad (4)$$

$$\frac{\partial H}{\partial y} = \frac{1}{\rho} \frac{\partial P}{\partial y} + u \frac{\partial u}{\partial y} + v \frac{\partial v}{\partial y} \quad (5)$$

Combining Eqs. (1) and (4), and (2) and (5) for an irrotational flow field yields the following equations,

$$-\frac{\partial H}{\partial x} = \frac{\partial u}{\partial t} \quad (6)$$

$$-\frac{\partial H}{\partial y} = \frac{\partial v}{\partial t} \quad (7)$$

which describe the flow field upstream of the rotor.

The boundary conditions imposed on the upstream perturbation flow field are that: (1) the perturbation velocity vanishes far upstream, (2) the side boundaries, which represent a common axial trace in the compressor flow, are taken as periodic (i.e., any flow leaving one side boundary must enter the other side boundary with the same velocity vector), and (3) the boundary condition at the rotor face is a prescribed potential distribution $\phi(y)$ at the initial time which represents the perturbation velocity. A new potential distribution $\phi(y)$ at this boundary is calculated at each time step. The solution to Laplace's equation with this boundary condition yields an expression for the axial perturbation velocity at the rotor upstream face.

The flow field downstream of the rotor can be modeled in a similar manner with the exception that the flow can no longer be considered irrotational. Vorticity introduced at the rotor semi-actuator disk will be convected downstream,

making the flow rotational. The downstream flow can then be described by a stream function $\psi(x,y,t)$ and a vorticity distribution $\zeta(x,y,t)$. The vorticity is distributed in the flow field downstream of the blade row and the equations of motion take the form of

$$-\frac{\partial H}{\partial x} = \frac{\partial u}{\partial t} - (V + v) \zeta \quad (8)$$

$$-\frac{\partial H}{\partial y} = \frac{\partial v}{\partial t} + (U + u) \zeta \quad (9)$$

Elimination of H from equations (8) and (9) yields

$$\frac{\partial \zeta}{\partial t} + (U + u) \frac{\partial \zeta}{\partial x} + (V + v) \frac{\partial \zeta}{\partial y} = 0 \quad (10)$$

In developing an equation to represent the exchange of energy between the rotor and the flow field, the time-dependent energy equation for a control volume is considered in the form

$$\rho Q (H_1 - H_2 - H_{loss}) = \rho s l \cos \xi \left(\frac{\partial Hc.v.}{\partial t} + \frac{\partial Hc.v.}{\partial y} \right) \quad (11)$$

where the H_{loss} term is the dynamic value of the rotor row losses. The control volume considered for Eq. (11) has sides parallel to the flow direction and to the blade pitch, and is equal to the blade pitch in width along the circumferential direction. The terms on the left hand side of the equation represent the fluid head of the flow entering the control volume, the fluid head of the flow leaving the control volume, and the total fluid head loss in the control volume due to viscous effects. The terms on the right hand side of the equation represents the change in energy in the control volume and the change in position of the control volume as it moves relative to the stationary frame of reference. Since the flow is assumed incompressible, only the change in kinetic energy of the flow in the control volume need be considered. If the average velocity of the flow in the control volume is assumed to be in the direction parallel to the blade, the flow will then be at an angle ξ to the axis of the compressor and the time variation of the kinetic energy in the control volume is

$$\frac{\partial Hc.v.}{\partial t} = \frac{\partial}{\partial t} \left(\frac{1}{2} C_x^2 \sec^2 \xi \right) = C_x \sec^2 \xi \frac{\partial u}{\partial t} \quad (12)$$

The position variation of the kinetic energy in the control volume is

$$\frac{\partial Hc.v.}{\partial y} = BV \frac{\partial}{\partial y} \left(\frac{1}{2} C_x^2 \sec^2 \xi \right) = C_x \sec^2 \xi \cdot BV \frac{\partial u}{\partial y} \quad (13)$$

Including this result in the time-dependent energy equation yields:

$$H_1 - H_2 - (H_{loss}) = k \left(\frac{\partial u}{\partial t} + BV \frac{\partial u}{\partial y} \right) \sec \xi \quad (14)$$

Taking the derivative of this equation in the tangential direction yields for the semi-actuator

disk

$$\frac{\partial H_1}{\partial y} - \frac{\partial H_2}{\partial y} - (H_{loss}) = k \sec \xi \left(\frac{\partial^2 u}{\partial y \partial t} + BV \frac{\partial^2 u}{\partial y^2} \right) \quad (15)$$

and

$$v_2 = -u \tan \beta_2 \quad (16)$$

Combining equations (8), (9), (15), and (16) yields

$$\frac{\partial v_1}{\partial t} = \frac{\partial}{\partial t} (-u \tan \beta_2) + (U + u) \zeta_2 - \frac{1}{2} \frac{\partial}{\partial y} (\omega_{dyn} w_1^2) - k \sec \xi \left(\frac{\partial^2 u}{\partial y \partial t} + BV \frac{\partial^2 u}{\partial y^2} \right) \quad (17)$$

where

$$\frac{1}{2} \frac{\partial}{\partial y} (\omega_{dyn} w_1^2) = H_{loss}$$

and

$$\omega_{dyn} = F^{-1} [TF \times F(\omega)_{quasi-steady}] ,$$

as previously discussed. Equation (17) then gives the time-variation of v_1 for the rotor.

The Downstream Flow Field Model

The two-dimensional flow field downstream of the rotor row is assumed to be incompressible, inviscid, and rotational, since the vorticity at the semi-actuator disk representing the rotor is convected downstream. The flow downstream of the rotor row can be described by a stream function $\psi(x,y,t)$ and a vorticity distribution $\zeta(x,y,t)$. The equations describing the downstream flow field are

$$\nabla^2 \psi = -\zeta \quad (18)$$

and

$$\frac{\partial \zeta}{\partial t} + \bar{u} \frac{\partial \zeta}{\partial x} + \bar{v} \frac{\partial \zeta}{\partial y} = 0 \quad (19)$$

where

$$\bar{u} = U + u$$

$$\bar{v} = V + v$$

$$\zeta = \frac{\partial \bar{v}}{\partial x} - \frac{\partial \bar{u}}{\partial y}$$

The solution of these equations is performed by using a finite difference technique throughout the flow field. Since \bar{u} and \bar{v} are known leaving the rotor row, the vorticity can be calculated. Far downstream from the rotor row, the boundary condition imposed is

$$\frac{\partial p}{\partial y} = 0 \quad (20)$$

The numerical solution of the downstream flow field is performed through the use of a successive overrelaxation technique.

Once the flow field is determined, a pressure solution is performed by solving the Poisson pressure equation

$$\nabla^2 p = 2 \left[\frac{\partial^2 \psi}{\partial x^2} \frac{\partial^2 \psi}{\partial y^2} - \left(\frac{\partial^2 \psi}{\partial x \partial y} \right)^2 \right]. \quad (21)$$

Results

The model may be utilized to develop solutions for the unsteady flow fields upstream and downstream of the rotor actuator disk. Input data are the quasi-steady loss and turning of the modeled rotor blade cascade, as determined from cascade tests or numerical calculations. Figure 2 shows a loss curve developed from available data for a 65 series cascade at 25° stagger angle. In addition, rotor blade velocity BV, blade row dimensions and inlet air density are specified.

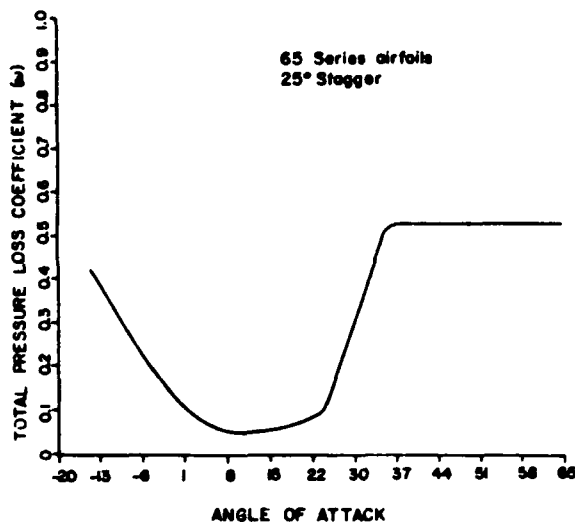


Fig. 2 Loss Curve for 65 Series Cascade

The initial flow field for the model is established by specifying an angle of attack for the flow over the rotor blades. This value, with the specified geometric parameters, generates a mean axial velocity which is maintained throughout a simulation run. The solution proceeds through small steps in time, developing perturbation values of velocities (u and v). If an initial small circumferential velocity perturbation grows for the specified angle of attack, a rotating stall is simulated. If the perturbation becomes smaller, the specified angle of attack will not produce rotating stall in the model, and is therefore considered to be less than the "inception" value.

Since the model calculates local velocity and pressure for the flow field in the region of the rotor, the variation of these values can be examined at each axial station in the flow field.

Sample results were developed for a blade row having loss characteristics as shown in Fig. 2, and for an initial angle of attack of 29°. This was well into the rotating stall region for this blade row, as the "inception" point was found in successive runs to be near 26°. Figure 3 shows the variation in axial velocity immediately upstream of the rotor as the stall develops and becomes stable. Forty-nine nodes in the circumferential direction were provided in the numerical formulation, representing 0-2 π radians around an annulus. The initial imposed perturbation is shown as a dashed line, while the final stable rotating velocity field is shown as a bold solid line. Other velocity plots in Fig. 3 represent the growing perturbation, and the continuing stable axial velocity disturbance representing a rotating stall. The simulated rotating stall is moving at a rate corresponding to approximately 45% of the blade velocity.

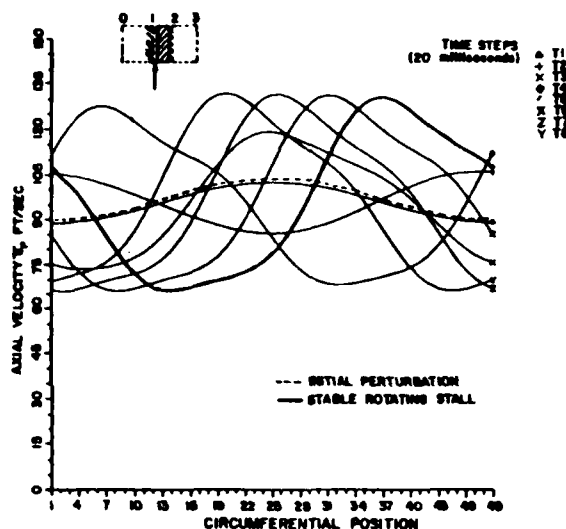


Fig. 3 Axial Velocity in Front of Rotor, Station 1

The local angle of attack of the flow at the rotor face, shown in Fig. 4, is the determining variable for the look-up of quasi-steady loss and turning angle values. The dynamic loss term ω_{dyn} of Eq. (17) is formed through the use of a response function.⁶

The associated tangential or circumferential velocity field immediately upstream of the rotor is shown in Fig. 5. The blockage of the stalled rotor passages induces a variation in tangential velocities as shown. Figure 6 shows the tangential velocity perturbations downstream of the rotor actuator disk, now relatively smaller because of the swirl velocity induced by the rotor. The varying pressure distribution around the simulated annulus downstream of the rotor is shown in Fig. 7, as calculated from Eq. (21). The static pressure pattern behind the rotor arises as a consequence of the varying vorticity field behind the rotor. The downstream pressure distribution changes from the pattern shown in Fig. 7 to a uniform pressure far downstream of the rotor, in accordance with the condition $\partial p / \partial y = 0$, imposed by Eq. (20).

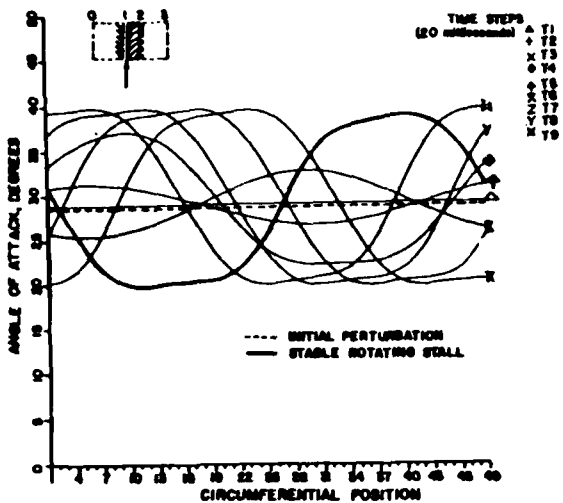


Fig. 4 Angle of Attack of Rotor Face, Station 1

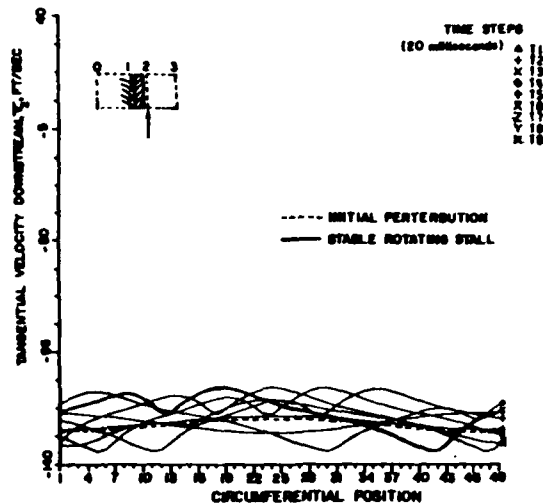


Fig. 5 Tangential Velocity Behind the Rotor, Station 2

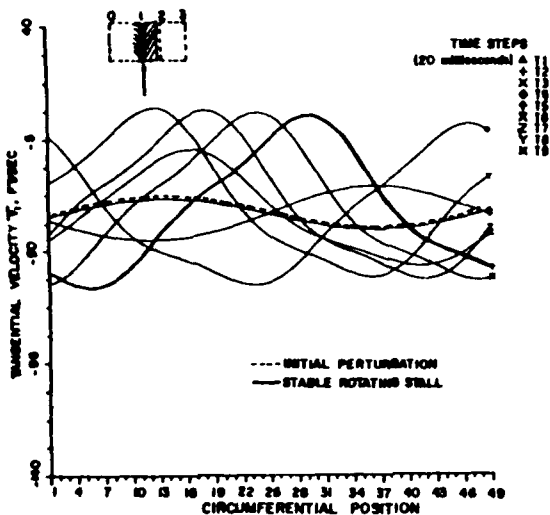


Fig. 6 Tangential Velocity in Front of Rotor, Station 1

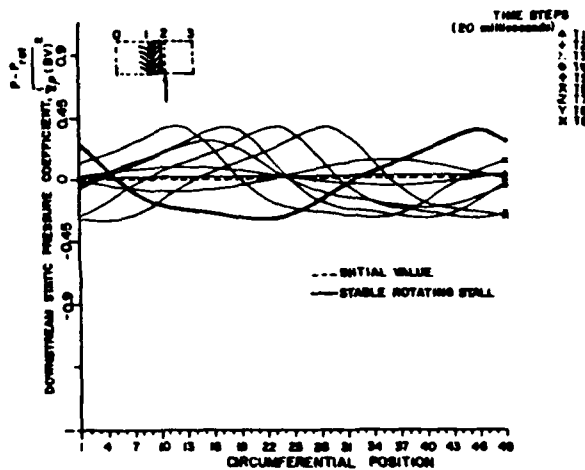


Fig. 7 Static Pressure Distribution Behind Rotor

Employing the simulation, it is possible to plot axial and tangential velocity distributions, as well as static pressure variations at any desired point in the modeled flow field, upstream or downstream of the rotor. The plots are useful for study of the rotating stall phenomenon, as well as for comparisons with measured values from modeled compressor stages.

Using the flow field pressures and velocities provided by the model, it is possible to construct a predicted compressor stage characteristic from the results of the simulation. The generally expected form of the rotating stall compressor characteristic is shown in Fig. 8. Study of the figure shows that stable operation on a throttle line within the bounded region is possible at two points. The actual point of operation depends upon the immediate past history of the compressor,

assuming that strong externally-imposed transients do not occur. Thus, a compressor in stable operation in a rotating stall will remain in rotating stall, so long as the throttle-imposed flow coefficient is within the range of the rotating stall characteristic. Similarly, a compressor in "normal" operation in the dual stability region will remain in normal operation unless the flow coefficient is reduced below the "inception" value, or the compressor operation is upset in some way, such as by a strong transient or an inlet distortion. The existence of a dual stability region, bounded by the stall inception and recovery lines, is the essential feature of recovery hysteresis. A measure of recovery hysteresis might be defined as

$$R = \frac{\bar{\phi}_B - \bar{\phi}_A}{\bar{\phi}_I} \quad (22)$$

with a low value of R representing good recovery characteristics.

The present calculation produces an operating characteristic for the modeled stage which is similar in form to that discussed above. It will be recalled that the boundary condition far downstream of the rotor requires a uniform static pressure in the circumferential direction. Since the local velocities at this point are also known, a mass-averaged total pressure can be conveniently calculated. The total pressure rise of the stage at each calculated operating point can thus be expressed in the form of a pressure coefficient,

$$\bar{\psi} = \frac{P_{03} - P_0}{\frac{1}{2} \rho (BV)^2}, \quad (23)$$

where the station numbers refer to Fig. 1

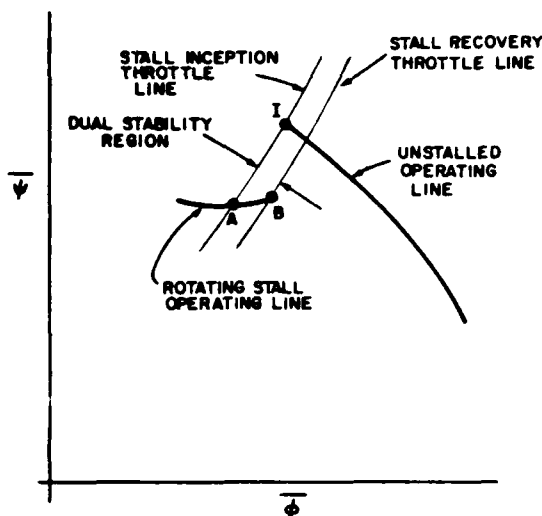


Fig. 8 General Form of Compressor Characteristic with Rotating Stall.

Specification of an initial angle of attack, inlet guide vane discharge angle, and rotor blade velocity produce a calculated steady axial velocity U , which is maintained as a convergence requirement throughout a given calculation. Axial velocity perturbations (u) developed by the computations are added to the constant mean axial velocity (U) to obtain the local absolute axial velocity,

$$\bar{u} = u + U. \quad (24)$$

Defining an average flow coefficient

$$\bar{\phi} = \frac{\int_0^{4\theta} \bar{u} dy}{BV(\Delta y)} = \frac{U}{BV}, \quad (25)$$

it can be seen that a given calculation will take place at a constant $\bar{\phi}$. Thus, the calculation simulates the development of a rotating stall cell at constant mass flow or $\bar{\phi}$, rather than along a fixed throttle line, as would occur in a conventional compressor test. A series of calculations are necessary to develop the rotating stall operating line, each defined by an initial angle of attack of the rotor flow. The calculation proceeds from the uniform axisymmetric flow condition at inception along a line of constant $\bar{\phi}$, to the fully-developed rotating stall simulation.

Figure 9 shows a stage operating characteristic developed from a series of eight runs of the computer model. Again, the loss curve of Fig. 2 was used, and a blade velocity of 166 feet per second was specified. For initial angles of attack of 25° or less, the imposed axial velocity perturbation decreased in magnitude, predicting stable, unstalled operation. For an initial angle of attack of 26° , the initial perturbation grew to a final stable velocity disturbance, moving at approximately 45% of blade velocity. Following the procedures described above, the values

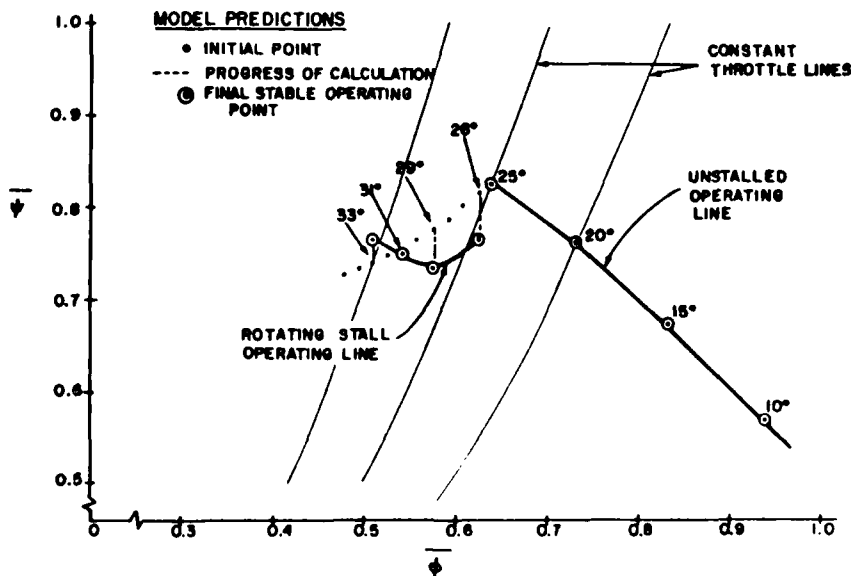


Fig. 9 Model-Generated Compressor Stage Unstalled and Post-Stall Characteristic; Input Data for 65 Series Cascade, 25° STAGGER.

of $\bar{\psi}$ and $\bar{\phi}$ were calculated for the starting point and the final stable rotating stall operating point. Additional calculations at 29°, 31°, and 33° initial angle of attack were performed, defining the predicted post-stall operating line shown in Fig. 9. The starting points for each calculation define a line of axisymmetric, but unstable, operation of the stage in the stalling regions of $\bar{\phi}$.

Constant throttle position lines are sketched in Fig. 9. The predicted inception and recovery throttle positions are labeled, leading to an estimate of the recovery parameter $R = 0.05$. Relatively small recovery hysteresis is evident here, as would be expected for the simple stage modeled. As can be seen from the geometry of Fig. 9, the use of input loss curves having a greater difference between the minimum and maximum loss values would lead to an operating line in stable rotating stall which is positioned lower on a graph such as Fig. 9. Predicted recovery hysteresis in the form of the recovery parameter R would therefore increase.

In several runs of the model, the shape of the loss curve in the transition region from low to high loss has been shown to affect the predicted inception point for rotating stall. Thus, a loss curve of the form shown in Fig. 10 would lead to a prediction of decreased angle of attack for stall inception, a less abrupt change in the operating line, and lower recovery hysteresis. Figure 11 shows a stage characteristic generated from the loss curve of Fig. 10, with all other parameters held constant. Reduced vertical spacing of the pre-stall and post-stall operating lines is evident, and improved recovery behavior is predicted. Here, the R -parameter is calculated as essentially zero, quantifying the improved recovery prediction.

The model is two-dimensional, and is limited in prediction accuracy by this assumption. The well-known tip-stalling behavior of a single

stage, leading to a "progressive", rather than an abrupt transition to rotating stall, is not simulated. The predicted behavior is more closely related to the full span stalling behavior observed in the stages of multistage compressors. While three-dimensional effects cannot be included in the present formulation, extension to include local reverse-flow calculation capability as well as the addition of a downstream stator row is possible.

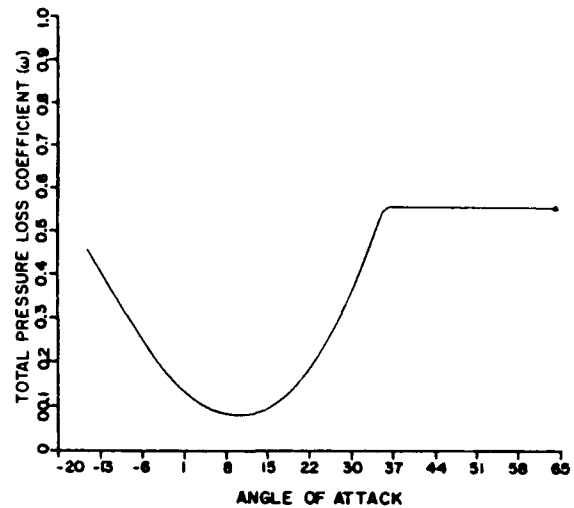


Fig. 10 Modified Loss Curve

Conclusions

A mathematical model for the two-dimensional unstalled and stalled flow in the neighborhood of a compressor stage composed of an inlet guide vane row and a rotor row has been described. Principal input data for the model are the rotor row quasi-

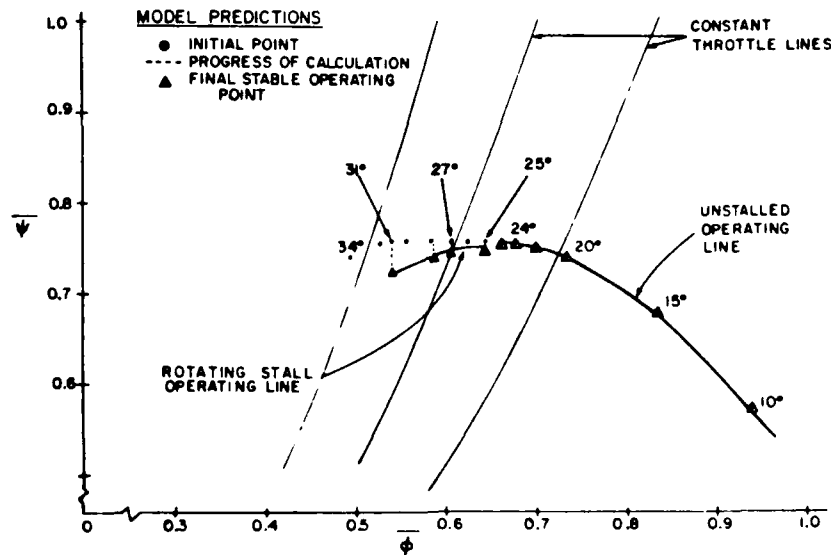


Fig. 11 Model-Generated Compressor Stage Unstalled and Post-Stall Characteristic, Modified Loss Curve

steady loss and turning angle data, a dynamic loss response function, the blade arrangement in terms of stagger and chord, and the rotor blade tangential velocity. Predictions of local velocity and pressure fields in rotating stall are obtained. A compressor stage performance map is predicted, including stable pre-stall and post-stall operating lines, and a measure of recovery hysteresis is suggested. The principal influence on model predictions is found to be contained in the shape of the rotor loss curve.

Acknowledgment

Support for this work was provided by the Air Force Office of Scientific Research, Bolling Air Force Base, D.C.

References

1. Johnsen, I. A., and R. O. Bullock, ed., Aerodynamic Design of Axial-Flow Compressors, NASA SP-36, 1965, pp. 331-364.
2. Greitzer, E. M., "Surge and Rotating Stall in Axial Flow Compressor. Part I: Theoretical Compression System Model," ASME Journal of Engineering for Power, Vol. 98, April 1978.
3. Day, I. J., E. M. Greitzer, and N. A. Cumpsty, "Prediction of Compressor Performance in Rotating Stall," Journal of Engineering for Power, Vol. 100, 1978.
4. Moore, F. K., "A Theory of Rotating Stall of Multistage Axial Compressors," NASA CR-3685, July 1983.
5. Takata, H., and S. Nagano, "Nonlinear Analysis of Rotating Stall," Journal of Engineering for Power, October 1972.
6. Sexton, M. R., and W. F. O'Brien, "A Model for Dynamic Loss Response in Axial-Flow Compressors," ASME Paper 81-GT-154, March 1981.

END

DATE

FILMED

DEC.

1987